



### 저작자표시-비영리-변경금지 2.0 대한민국

이용자는 아래의 조건을 따르는 경우에 한하여 자유롭게

- 이 저작물을 복제, 배포, 전송, 전시, 공연 및 방송할 수 있습니다.

다음과 같은 조건을 따라야 합니다:



저작자표시. 귀하는 원 저작자를 표시하여야 합니다.



비영리. 귀하는 이 저작물을 영리 목적으로 이용할 수 없습니다.



변경금지. 귀하는 이 저작물을 개작, 변형 또는 가공할 수 없습니다.

- 귀하는, 이 저작물의 재이용이나 배포의 경우, 이 저작물에 적용된 이용허락조건을 명확하게 나타내어야 합니다.
- 저작권자로부터 별도의 허가를 받으면 이러한 조건들은 적용되지 않습니다.

저작권법에 따른 이용자의 권리와 책임은 위의 내용에 의하여 영향을 받지 않습니다.

이것은 [이용허락규약\(Legal Code\)](#)을 이해하기 쉽게 요약한 것입니다.

[Disclaimer](#)



Ph. D DISSERTATION

A STUDY ON RF/MICROWAVE

APPLICATIONS:

MAGNETIC FLUID HYPERTERMIA

AND BRAIN STIMULATION

무선 및 초고주파의 응용에 관한 연구:  
자기 유체 온열요법과 뇌 자극

BY

TAEYOON SEO

AUGUST 2018

SCHOOL OF ELECTRICAL ENGINEERING AND  
COMPUTER SCIENCE COLLEGE OF ENGINEERING  
SEOUL NATIONAL UNIVERSITY

A STUDY ON RF/MICROWAVE APPLICATIONS:  
MAGNETIC FLUID HYPERTHERMIA  
AND BRAIN STIMULATION

지도 교수 서 광 석

이 논문을 공학박사 학위논문으로 제출함

2018년 8월

서울대학교 대학원

전기·컴퓨터 공학부

서태윤

서태윤의 공학박사 학위논문을 인준함

2018년 8월

위원장 남상옥 (인)

부위원장 서광석 (인)

위원 권영우 (인)

위원 천창율 (인)

위원 조제원 (인)

## Abstract

In this dissertation, studies on magnetic fluid hyperthermia and brain stimulation as an application field of RF/microwave are presented.

In the first chapter, a magnetic fluid hyperthermia (MFH) has been studied. Magnetic, iron oxide, nanoclusters (MNCs) with regular size distribution and high stability were successfully prepared. In order to enhance the therapeutic effect of MNC, the process of finding optimal conditions was performed according to various factors, such as particle size distribution, external magnetic field frequency, and intensity. The correlation between heat generation ability and the various factors was evaluated by measuring the specific loss power (SLP). The 60 nm MNC showed the highest heat capacity ability in the various field conditions. Breast cancer stem cells (bCSCs) with chemo/radio-resistance were exposed to the optimized alternating magnetic field after treating with the MNC. The MNC promoted an appropriate temperature increase within 10 min. Thus, the treated CSCs were progressed to the thermal-mediated apoptotic cell death.

When MNCs are injected into a biological tissue for MFH therapy, cell and *in vivo* experiments cannot guarantee the same effects because of metabolic, blood volume, or rate. The synthesized MNCs suitable for MFH were injected directly into the middle of tumor tissue of nude mice. Since the micro-environment of the MNC has changed, the magnetic field conditions have changed to achieve a therapeutic effect. The intensity of magnetic field has changed with the temperature change of the biological tissue. It has been shown that tumor volume decreases after MFH treatment. However, total tumor tissue was not treated. To increase the therapeutic effect, the same amount of the MNC was injected into various sites of cancer tissues

of the other mouse. As a result, it was visually confirmed that the tumor tissue was destroyed without damage to healthy tissues.

As a second study, the results of neuronal stimulation using electromagnetic fields are presented. A conventional transcranial magnetic stimulation (TMS) system was improved by using a full-bridge inverter circuit. The proposed TMS system can control the pulse width and generate a complex brain stimulation protocol. We then tested if TMS modulate nociceptive behaviors. A new TMS protocol mimicking thalamic burst firing patterns was tested for endogenous thalamocortical (TC) activity. The experimental results showed that nociceptive behaviors decreased after applying the TMS.

The proposed TMS system modulates the envelope of continuous signal to produce thalamic burst firing patterns. The study continues to investigate whether the envelope modulated microwave signal affects the firing rate of neurons. Microwaves were used to narrow the electromagnetic field distribution and modulate brain activity with less power than conventional brain stimulation methods such as a TMS. Microwave circuits for the brain stimulation system were developed by MMIC technology and semiconductor manufacturing process. *in-vivo* experiments confirmed that microwave signals with repetitive pulse envelopes successfully changed the activity of individual neurons.

In this dissertation, it was shown that RF/microwave can increase the temperature of biological tissue through energy conversion agent, MNCs. Through this, cancer treatment can be expected. This dissertation has also demonstrated the possibility that modulation of the signal can be practically applied to control brain activities.

**Keywords :** magnetic fluid hyperthermia, magnetic nanoparticle, magnetic field

generator, transcranial magnetic stimulation, neuromodulation, noninvasive brain stimulation, microwave brain stimulation, stimulation applicator.

**Student number :** 2011-30963

# **Contents**

**Abstract** ..... **i**

**Contents** ..... **iv**

**List of Figures** ..... **vi**

**List of Tables** ..... **xii**

**Chapter 1 Introduction** ..... **1**

**Chapter 2 Magnetic Fluid Hyperthermia** ..... **3**

2.1	Introduction	3
2.2	Magnetic Nanocluster	5
2.3	Magnetic Field Generator	10
2.3.1	Solenoid Coil	10
2.3.2	Full-Bridge Inverter	15
2.4	SLP Measurement	18
2.5	Cancer Cell Experiments	23
2.6	Mouse Experiments	30

**Chapter 3 Brain Stimulation** ..... **38**

3.1	Introduction .....	38
3.2	Transcranial Magnetic Stimulation .....	40
	3.2.1 Pulse envelope modulated AMF generation system .....	41
	3.2.2 Mouse Experiment .....	48
3.3	A New Brain Stimulation Method Using Microwave .....	53
	3.3.1 Pilot Demonstration .....	55
	3.3.2 Microwave Signal Generation Using MMICs .....	61
	3.3.3 Waveform Modulation and Power Amplification .....	64
	3.3.4 Integrated Brain Stimulation System .....	66
	3.3.5 Stimulation Applicator .....	69
	3.3.6 Mouse Experiments .....	72
<b>Chapter 4</b>	<b>Conclusion .....</b>	<b>78</b>
<b>Appendix</b>	<b>.....</b>	<b>81</b>
	Fields of Finite Solenoid Coil – calculation of off the axis .....	82
	High Resolution TEM Images .....	81
	Expression Levels of ALDH1 and CD44+/CD24- during MFH treatment .....	82
	Expression Levels of HSP70 and HSP90.....	94
<b>References</b>	<b>.....</b>	<b>96</b>
<b>Abstract in Korean (국문초록)</b>	<b>.....</b>	<b>105</b>

## List of Figures

Fig. 1. Concept of magnetic fluid hyperthermia .....	4
Fig 2. TEM images of the synthesized magnetite MNCs with mean diameters of 30, 40, and 60 nm. ....	5
Fig 3. Size distribution of 60 nm MNC obtained through DLS analysis. ....	6
Fig. 4. Minor AC hysteresis loops of MNCs obtained by varying the frequency from 10 kHz to 500 kHz at a field intensity of 1 kA/m. (a) Whole hysteresis curves. (b) Expanded curves. (The symbols in the graph do not represent measurement points.)	7
Fig. 5. (a) Block diagram of a magnetic field generator .....	10
Fig. 6. Schematic of the solenoid with N turns. ....	11
Fig. 7. Magnetic field distribution of the solenoid (side view)....	13
Fig. 8. Magnetic field direction of the solenoid (side view).....	14
Fig. 9. (a) Schematic of Full-Bridge inverter circuit and (b) Full-bridge inverter module. ....	15
Fig. 10. (a) Solenoid coil model for 3D electromagnetic simulation. (b) Magnetic field distribution. (c) Experimental setup of the coil, MNC solution, and optical fiber probe. ....	17
Fig. 11. SLP of MNCs. The frequencies are (a) 289, (b) 387, (c) 756, and (d) 1056 kHz. ....	19
Fig. 12. SLP per unit frequency. The field strengths are (a) 5.45 kA/m and (b) 6.45 kA/m. ....	22
Fig. 13. Characterization of mammosphere (MS) formation. ....	24

Fig. 14. MS formation. The size of the cultured MS at different days.....	25
Fig. 15. Confocal microscopic image of the MS cells treated with red fluorescent MNC particles and the floating cells after MNC treatment. ....	25
Fig. 16. Images from the infrared camera during AMF application at different times (heat scale unit: °C).....	26
Fig. 17. Temperatures generated by the MNCs of various sizes, media, and cell only (untreated) samples at different times.	27
Fig. 18. Cell viability at different concentrations of the MNCs in the absence of an AMF.....	28
Fig. 19. Cell viability at different treatment times of AMF.....	28
Fig. 20. Microphotographs of the cancer: (a) and (b) Hematoxylin and eosin (HE) staining, (c) and (d) Prussian blue staining..	31
Fig. 21. Experimental settings: (a) The mouse lay inside the jig. The cancer tissue is at the center of jig. (b) The IR camera measures the skin temperature of the mouse. .....	32
Fig. 22. (a) Photographs of the IR camera, (b) the optical fiber thermometer results. (The symbols in the graph do not represent measurement points.) .....	33
Fig. 23. Photographs of cancer tissue of nude mice. ....	34
Fig. 24. (a) Photographs of IR camera, (b) the fiber optic thermometer results. (The symbols in the graph do not represent measurement points.) .....	35
Fig. 25. Photographs of the tumor treated with MFH. ....	36

Fig. 26. The cancer volumes for control, sham-treated, MFH treated group were plotted as a function of time.....	37
Fig. 27. The existing TMS system and the newly proposed pulse envelope TMS system.....	42
Fig. 28. Block diagram of proposed TMS system. ....	42
Fig. 29. The waveform of the proposed stimulation system.....	43
Fig. 30. (a) Upper pillar and (b) lower plate of the supporting stand. ....	44
Fig. 31. Fabricated stimulus coil.....	45
Fig. 32. Mouse with lower plate of supporting stand (left) and stimulation coil.....	45
Fig. 33. Magnetic field distribution of the solenoid (side view)..	46
Fig. 34. Electric field distribution of the solenoid (top view, at z = 5 mm).....	46
Fig. 35. Electric field distribution of the solenoid (top view, at z = 7 mm).....	47
Fig. 36. Schematic drawing of TMS coil placement.....	48
Fig. 39. Acute thermal nociception changes triggered by TMS protocols. Paw withdrawal latency to plantar paw IR irradiation (Kruskal-Wallis test with Mann-Whitney U test; n = 6 mice per group). .....	51
Fig. 40. Formalin-induced inflammatory nociceptive behavior changes to different TMS protocols (repeated measures ANOVA followed by Games Howell post hoc; n = 6 mice per group).....	52

Fig. 41. Concept of brain stimulation via modulated microwave signal.....	54
Fig. 42. (a) Conventional and planar type coaxial line, (b) structure of proposed applicator, and (c) photograph of the aperture.	56
Fig. 43. Measured S-parameter of the applicator.....	57
Fig. 44. Experimental setup for brain stimulation using the microwave.....	57
Fig. 45. (a) Experimental setup of mouse, (b) applicator and nichrome wire of micro-drive.....	59
Fig. 46. The stimulation results. The firing rate was measured using micro-drive.....	59
Fig. 47. Overall block diagram of the proposed brain stimulation system.....	61
Fig. 48. A schematic of the designed VCO and buffer amplifiers. VCO is made up of n-type MOS and p-type MOS cross-coupled pair and a LC tank.....	62
Fig. 49. A buffer amplifier has variable load. Equivalent load impedance has a value between R2 and R1//R2 depending on the state of the transistor M1. ....	63
Fig. 50. Schematic diagram of the designed PA and transformer. ....	64
Fig. 51. (a) Cross-sectional view of the seven-layer PCB, (b) layout of the transformer. ....	65
Fig. 52. Photograph of stimulation system. (a) Integrated IC and	

biasing PCB. (b) Enlarged photograph of the CMOS and transformer.....	66
Fig. 53. Measured results of the stimulation system. (a) Frequency tuning range, (b) output power.....	67
Fig. 54. The modulated microwave signal in time domain and frequency domain (a) measured result in time domain, (b) measured result in frequency domain.....	67
Fig. 55. Stimulation applicator. (a) Upper plane, (b) lower plane, (c) oblique view,.....	69
and (d) s-parameter of the simulation result. ....	69
Fig. 56. Experimental setup consisting of the proposed stimulation signal generator and an applicator.....	72
Fig. 57. (a) Photograph of the stimulation applicator and nichrome wires of a micro-drive. ....	73
(b) illustration to help understand the placement of the applicator and micro-drive.....	73
Fig. 58. Waveform of the modulated microwave signal used in this work. ....	74
Fig. 59. Cellular response to the modulated microwave signal. Positive value indicates excitation, while negative value indicates inhibition of neuronal activity. Normalization was based on the baseline firing rate. (N= 34 neurons, 4 mice in stimulation group; N=18 neurons, 4 mice in control group). 75	
Fig. 60. Changes in temperature in the hippocampus and on the brain surface when microwave energy is delivered to the brain.	



## List of Tables

Table I. Physical properties of the MNCs. The whole size, crystal size, Ms, and coercivity were determined by through TEM, XRD, and MPMS [17] .....	6
Table II. Measured coercivity at different frequencies from 10 to 500 kHz at a field intensity of 1 kA/m.....	8
TABLE III. Neuronal activities of each sessions.....	76

# Chapter 1 Introduction

For several decades, hyperthermia has been major subjects of interest in investigating the biological effects and applications of microwaves. More recently, other subjects have also received attention, i.e., power absorption in human subjects[1], interaction with the nervous system[2], influence of extremely low-frequency-modulated fields on membrane channels[3], and molecular effects[4]. In *in vivo* absorption experiments, there is evidence that RF/microwaves directly affect living systems. There are ambiguities, however, concerning the relative contributions of specific and indirect thermal effects, and the possibility of direct non-thermal interactions. Unambiguous evidence of direct effects is provided by *in vitro* studies, revealing effects at various frequencies and intensities, on a number of cellular endpoints, including calcium binding, proliferation, ligand-receptor-mediated events, and alteration in membrane channels. Interactions occurring at the microscopic level are related to the dielectric properties of biological macromolecules and molecular assemblies, in the form of functional units such as enzyme complexes, cell-membrane receptors, or ion channels. Three handbooks provide a good background in the field. Michaelson and Lin [4]review biological effects, Thuery [5] describes the industrial, scientific, and medical applications, and Polk and Postow [6] review biological effects. European research was reviewed in 1993 [7]. A detailed discussion of some of the topics related to microwave therapeutic medicine could be found in [8].

In this dissertation, hyperthermia has been studied based on magnetic materials that convert magnetic energy into thermal energy. This dissertation also describes

the effect of the electromagnetic field used in hyperthermia on the brain neuronal activity. In addition, a new method of controlling brain activities by modulating continuous microwave signal has been proposed.

# **Chapter 2 Magnetic Fluid Hyperthermia**

## **2.1 Introduction**

In the past few decades, there have been numerous studies and efforts toward treating cancer. Hyperthermia therapy is a treatment that increases the temperature of tumors using external energy such as microwave and ultrasonic. However, it is difficult to increase the temperature of cancer tissues while suppressing the temperature of normal tissues. Magnetic fluid hyperthermia (MFH), which is one of the methods of using thermal seeds, is attracting considerable attention because it is advantageous for concentrating heat only locally [9, 10]. Magnetic nanoparticles have been studied for several years in various applications such as magnetic resonance imaging (MRI) contrast agents, drug delivery, and MFH.

Among the numerous properties of magnetic nanoparticles, a few noteworthy features can be used for MFH. First, they convert external magnetic energy into heat by combining several mechanisms[11]. The magnetic field outside a body can induce apoptosis or necrosis by increasing the temperature of the nanoparticles located in cancer tissues. Second, they can be synthesized at several nm sizes. At this size, cells can uptake nanoparticles. Third, the surface coating is possible[12]. Antibody-coated nanoparticles can be combined with cancer cells, making them an excellent local cancer treatment. Fig. 1 illustrates a brief concept of this chapter. The magnetic material generating heat in the alternating magnetic field (AMF) can be synthesized as small as a nanometer size. Assuming that the antibody coated nanoparticles are injected into the tumor model with sufficient concentration, an external AC magnetic field can be used to raise the temperature of the tumor to achieve a therapeutic effect.

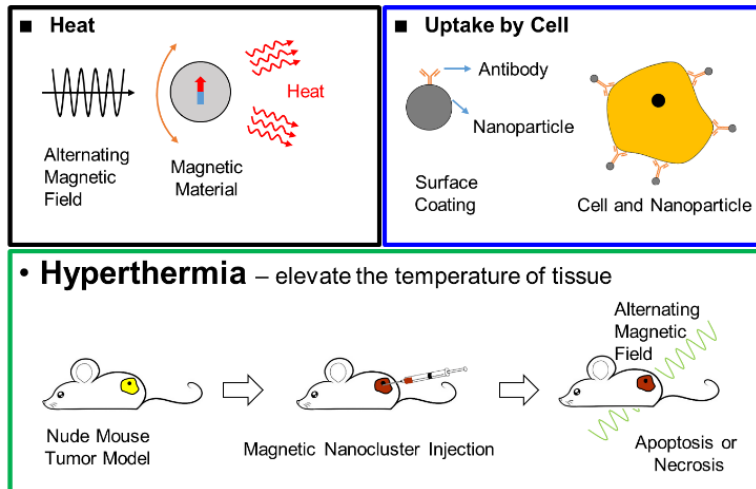


Fig. 1. Concept of magnetic fluid hyperthermia

Various materials are being tested for thermal seed of MFH. Typically, maghemite ( $\gamma\text{-Fe}_2\text{O}_3$ ) and magnetite ( $\text{Fe}_3\text{O}_4$ ) are used. The US food and drug administration (FDA) has approved these materials for use as contrast agents in MRI [13]. Superparamagnetic iron oxide nanoparticles (SPIONs) are suitable for *in vivo* MFH because they are easy to transport, exhibit good circulation, and have good colloidal stability. However, low heat generation is a major drawback of SPIONs [14]. To elevate the heat generation, studies have been carried out on the improvement of energy conversion characteristics using multicore nanoparticles [14-16]. Multicore nanoparticles have been proven to be effective by *ex vivo* [14] or cell experiments [16]. In this dissertation, the heating property of magnetic nanoparticles was optimized based on various magnetic field conditions. Based on optimized condition, the effect of hyperthermia was confirmed by cell and *in vivo* test.

## 2.2 Magnetic Nanocluster

Previous studies have synthesized clusters of iron oxide nanoparticles with various size distributions [17, 18]. The heating characteristics of synthesized nanoclusters depend on the frequency or intensity of a magnetic field [17]. We attempted to improve the effect of hyperthermia therapy by varying magnetic field conditions instead of changing the characteristics of iron oxide nanoparticles. We used  $\text{FeCl}_3$  as the iron source and ethylene glycol as a solvent and reductant to synthesize the nanoclusters according to known methods [17]. The size of the synthesized MNCs can be adjusted from 20 to 80 nm depending on the concentration of  $\text{FeCl}_3$  and sodium acetate. The prepared MNCs were coated with polyacrylic acid (PAA) to improve their stability in aqueous solution. A detailed description of the synthesis process can be found in [17]. Transmission electron microscope (TEM) analysis shows that the synthesized MNCs with sizes of 30, 40, and 60 nm are almost spherical, as shown in Fig 2. Depending on various factors such as the shape and size of nanoparticles, energy conversion is performed through different heat generation mechanisms.

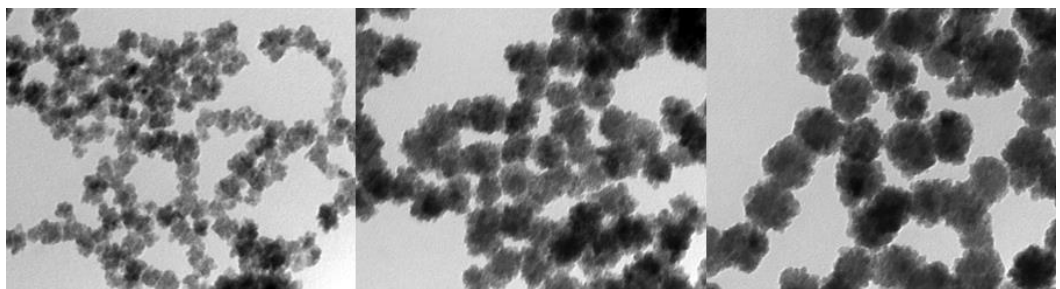


Fig 2. TEM images of the synthesized magnetite MNCs with mean diameters of 30, 40, and 60 nm.

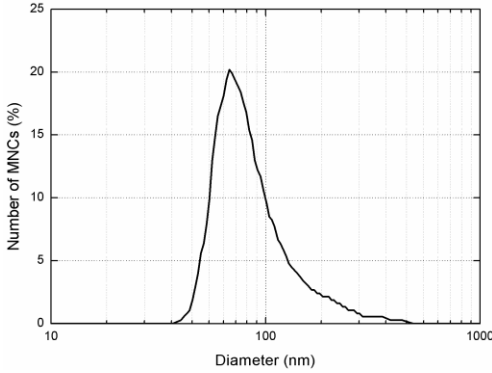


Fig 3. Size distribution of 60 nm MNC obtained through DLS analysis.

We analyzed the 60 nm MNC using dynamic light scattering (DLS) to obtain the size distribution. As shown in Fig. 3, the mean hydrodynamic diameter of the 60 nm MNC, including coating thickness and water molecules, is 91.42 nm.

Table I. Physical properties of the MNCs. The whole size, crystal size, Ms, and coercivity were determined by through TEM, XRD, and MPMS [17]

Whole size (nm)	Crystal size (nm)	Ms (emu/g [Fe])	Coercivity (A/m)
$20 \pm 4.1$	10.0	66.6	1018.60
$30 \pm 4.1$	9.9	63.4	915.14
$40 \pm 9.2$	9.9	63.3	859.44
$60 \pm 8.3$	19.8	69.2	1018.60
$80 \pm 7.5$	23.7	66.8	1034.51

Table I summarizes the magnetic and structural properties of the samples evaluated through X-ray diffraction (XRD) and the magnetic property measurement

system (MPMS-5XL, Quantum Design). The coercivity of the 60 nm MNC is 1018.6 A/m, which exhibits ferromagnetic nature. As pure superparamagnetic iron oxide nanoparticles show extremely low specific loss power (SLP) [19], we take advantage of the high heating properties using nanoclusters. As a result of obtaining apoptosis in the hyperthermia treatment of cancer stem cells using nanoclusters, positive results can be expected about cytotoxicity [17].

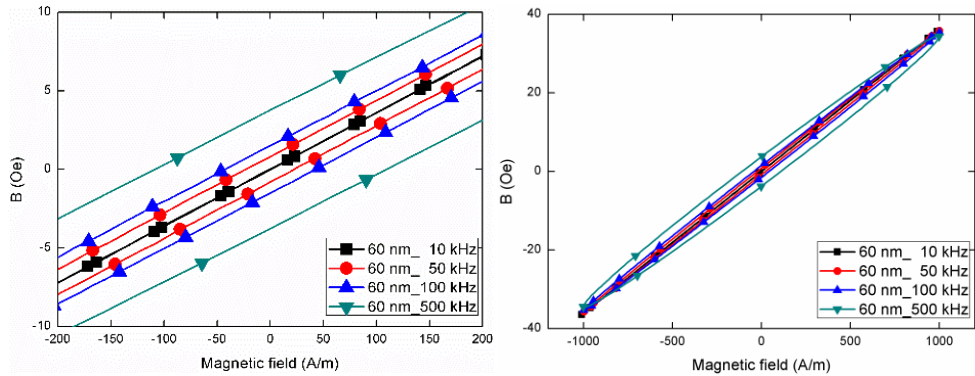


Fig. 4. Minor AC hysteresis loops of MNCs obtained by varying the frequency from 10 kHz to 500 kHz at a field intensity of 1 kA/m. (a) Whole hysteresis curves. (b) Expanded curves. (The symbols in the graph do not represent measurement points.)

In superparamagnetic iron oxide nanoparticles, relaxation loss is the dominant mechanism of heat generation, and hysteresis is prominent in ferromagnetic nanoparticles [19-22]. According to a previous study, the transition from Neel to Brownian rotation occurred at a particle size of 16 nm[13]. Given the size distribution of the synthesized nanoclusters, energy conversion can be expected to be caused by a combination of two relaxations and hysteresis loss [23-25]. We want

to improve the effect of hyperthermia by changing the frequency and intensity of a magnetic field. AC magnetization curves were measured to observe the change in magnetic characteristics. The curves were measured in a frequency range of 10 kHz to 500 kHz at a field intensity of 1 kA/m (Remacomp C-100, Magnet-physics INC). The minor hysteresis loop of the 60 nm MNC solution is dependent on frequency, as shown in Fig 4. In this frequency range, the coercivity of the MNCs tends to increase with frequency. In addition, the area enclosed by the hysteresis loop increases as remanence increases.

Table II. Measured coercivity at different frequencies from 10 to 500 kHz at a field intensity of 1 kA/m

MNC size (nm)	10 kHz	50 kHz	100 kHz	500 kHz
20 ± 4.1	0.288	26.3	45.37	113
30 ± 4.1	0.302	25.2	44.2	111
40 ± 9.2	0.415	27.4	47.4	114
60 ± 8.3	0.358	22.7	42.5	109
80 ± 7.5	0.304	24.2	43.4	110

Table II summarizes the coercivity obtained by measuring the AC magnetization curve for all nanoclusters. Coercivity changes significantly with frequency, as compared to nanoparticle size. As the magnetic field strength is limited to 1 kA/m when measuring the AC hysteresis loop, the measurement results do not reflect the overall characteristics of the nanoclusters. However, Table I also shows that there is no correlation between size and coercivity. Therefore, the results of frequency-

dependent coercivity are convincing. This is considered to be because the rotation of magnetic moment occurs later than the change in the applied field when the magnetic field changes faster than relaxation time [23-25].

## 2.3 Magnetic Field Generator

The configuration of the magnetic field generator is shown in Fig 5; it includes a full-bridge inverter, transformer, and a series LC resonant circuit. In this chapter, descriptions of each device constituting the magnetic field generator is given.

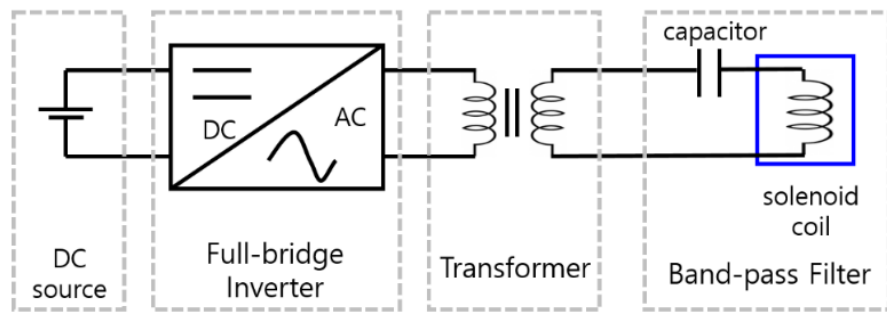


Fig. 5. (a) Block diagram of a magnetic field generator

### 2.3.1 Solenoid Coil

The solenoid coil produces a magnetic field with uniform distribution inside the solenoid coil. The field strength depends on the current amplitude and the number of the coil. The magnetic and induced electric field around the coil were calculated by solving a vector magnetic potential function based on the Biot-Savart law [26, 27]. A solution of the field equation is presented in terms of complete elliptic integrals at any point inside or outside a solenoid.

In the solenoid structure shown below, the magnetic flux density ( $\bar{B}$ ) generated when current flows through the coil is represented by the vector potential  $\bar{A}$  as follows.

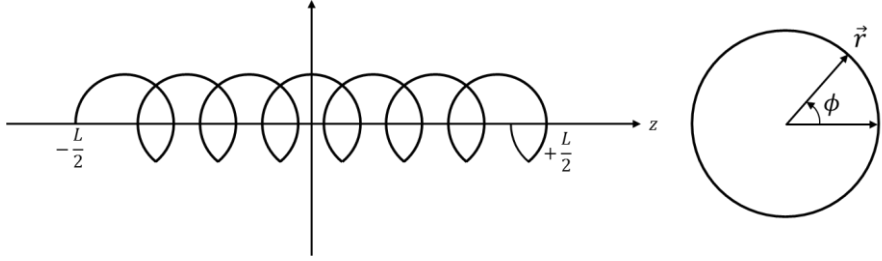


Fig. 6. Schematic of the solenoid with  $N$  turns.

$$\bar{B} = \nabla \times \bar{A} \quad (1)$$

where considering geometry, the only  $A_\phi$  term is left.

Therefore, Eq. (1) can be separated as follows.

$$B_r = -\frac{\partial A_\phi}{\partial z}, \quad B_z = \frac{1}{r} \frac{\partial (r A_\phi)}{\partial \rho} = \frac{1}{r} A_\phi + \frac{\partial A_\phi}{\partial \rho} \quad (2)$$

Neglecting the small current flowing in the  $z$ -axis direction in the Fig. 6, the current density  $\bar{J}$  has only a component in the  $A_\phi$  direction,

$$J_\phi = I \sin \theta' \delta(\cos \theta') \frac{\delta(r' - a)}{a} \quad (3)$$

The delta functions limit the current flow to a circumference of a radius  $a$ . The total current density can be written as below. [27]

$$\bar{J} = \bar{a}_x (-\sin \phi') J_\phi + \bar{a}_y (\cos \phi') J_\phi \quad (4)$$

Generally, the vector potential function  $A$  can be obtained by integrating the current density, Eq. (4) as follows.

$$A_\phi(\bar{x}) = \frac{\mu_0}{4\pi} \int \frac{\bar{J}(\bar{x}')}{|\bar{x} - \bar{x}'|} d^3x' \quad (5)$$

The process of obtaining the magnetic field from a finite solenoid is described in detail in the appendix. The final field expression is:

$$\begin{aligned} B_r &= -\frac{\mu_0}{\pi} \frac{Ia}{L} \frac{k}{2\sqrt{a\rho}} \int_0^{\frac{\pi}{2}} \frac{1 - 2\sin^2 \theta}{\sqrt{1 - k^2 \sin^2 \theta}} d\theta \\ &= -\frac{\mu_0}{\pi} \frac{I}{L} \sqrt{\frac{a}{\rho}} \left( \frac{k^2 - 2}{2k} K(k^2) + \frac{1}{k} E(k^2) \right)_{\zeta_-}^{\zeta_+} \end{aligned} \quad (6)$$

where  $K(x^2) = \int_0^{\frac{\pi}{2}} \frac{1}{\sqrt{1 - x^2 \sin^2 \theta}} d\theta$  and  $E(x^2) = \int_0^{\frac{\pi}{2}} \sqrt{1 - x^2 \sin^2 \theta} d\theta$  are the standard elliptic integrals of the first and second kind respectively.

$$B_z = -\frac{\mu_0 I}{4\pi L \sqrt{a\rho}} \left[ k \zeta \left( K(k^2) + \frac{a - \rho}{a + \rho} \Pi(h^2, k^2) \right) \right]_{\zeta_-}^{\zeta_+} \quad (7)$$

$$\text{where } h^2 = \frac{4a\rho}{(a+\rho)^2}, \quad k^2 = \frac{4a\rho}{(a+\rho)^2 + \zeta^2}, \quad \text{and}$$

$$\prod(n,m) = \int_0^{\frac{\pi}{2}} \frac{1}{(1-n\sin^2\phi)\sqrt{1-m\sin^2\phi}} d\phi. \text{ The last term is the standard elliptic integral of the third kind.}$$

So far, the magnetic field induced by the solenoid coil has been derived as a formula in terms of the complete elliptic integral. The electric field can be derived from the magnetic field using the Maxwell equations [26]. The dimension of solenoid is 4 mm  $\times$  10 mm (diameter  $\times$  height). Fig. 7 and Fig. 8 shows magnetic field distribution and direction around the solenoid, respectively. The magnetic field is maximum at the edge of the solenoid and falls rapidly as you move away.

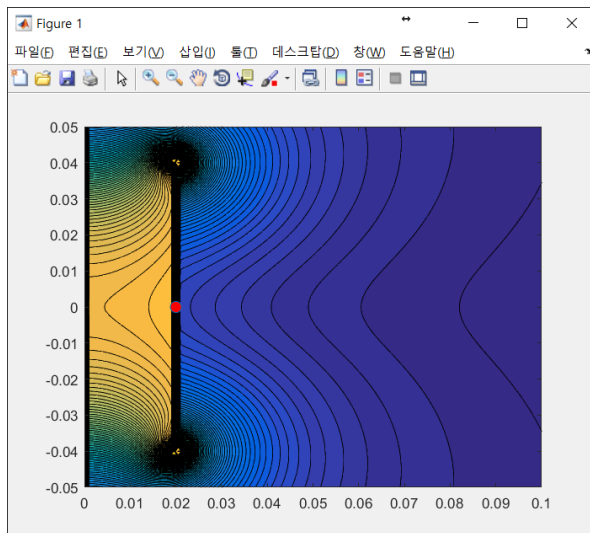


Fig. 7. Magnetic field distribution of the solenoid (side view).

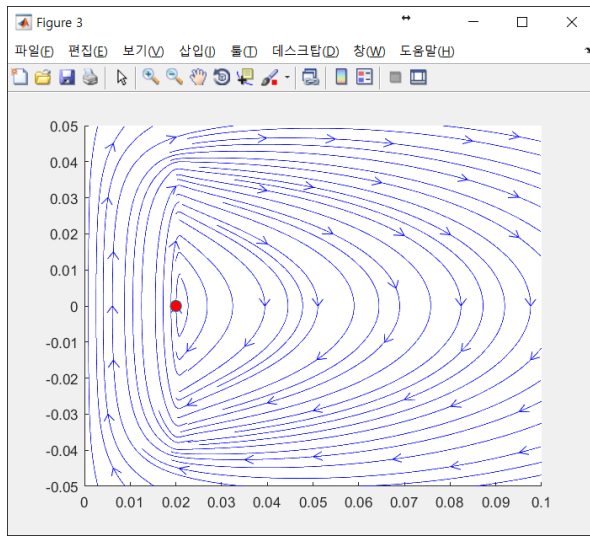


Fig. 8. Magnetic field direction of the solenoid (side view).

The solenoid coil is suitable for increasing the strength of the magnetic field, and it can evenly distribute the magnetic field to all portions of the MNC sample. The solenoid coil is built by winding a copper pipe 5.5 times with a coil diameter of 16 mm.

### 2.3.2 Full-Bridge Inverter

A full-bridge inverter circuit is used to generate alternating current; this is the simplest method of producing alternating current from direct current [28].

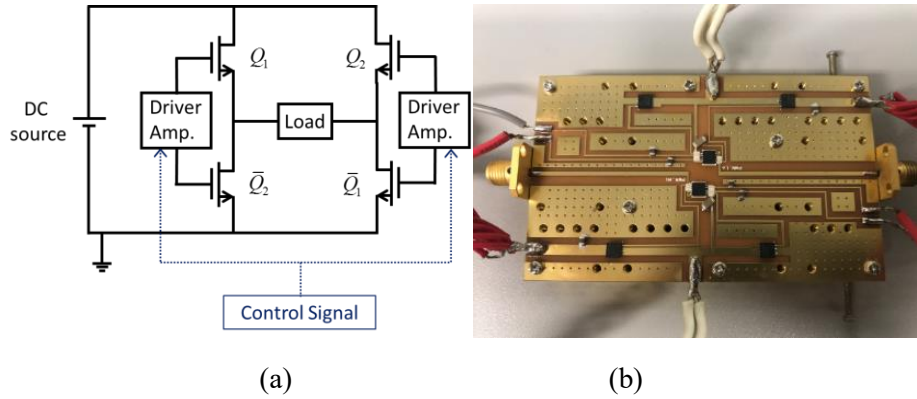


Fig. 9. (a) Schematic of Full-Bridge inverter circuit and (b) Full-bridge inverter module.

The inverter converts dc source to ac. The full-bridge inverter is a switching configuration circuit as shown in Fig. 9. An ac output is synthesized from a DC input by closing and opening switches  $Q_1$ ,  $\bar{Q}_1$ ,  $Q_2$ , and  $\bar{Q}_2$  in an appropriate sequence. When  $Q_1$  and  $\bar{Q}_1$  are turned on, the load current flows from left to right. When  $Q_2$  and  $\bar{Q}_2$  are turned on, the load current flows in the opposite direction. By controlling this sequence, an ac is produced at the load. A uniform magnetic field can be obtained by placing a solenoid coil on the load of the inverter

Generally, the intensity of the magnetic field is proportional to the amplitude of the current. Since the current magnitude of the inverter output is low, current amplification is required to increase the magnetic field strength. Transformer was used for current amplification. The high voltage output signal of the inverter is

delivered to the transformer. The transformer is used to convert high voltage and low current into a low voltage and high current. A capacitor–inductor series section forms a band-pass filter to cancel the impedance of the coil at the resonant frequency. If the inverter generates a signal with the same frequency as the resonant frequency of the filter, a strong magnetic field is formed in the coil. The resonant frequency of the filter must be changed to change the frequency of the magnetic field. Even if the resonance frequency is changed by changing the capacitance and the inductance, the solenoid coil is maintained so that the intensity of the magnetic field transmitted to the MUT (MNC solution in this dissertation) is maintained. The resonant frequencies used in the experiment are 289, 387, 459, 536, 620, 756, and 1056 kHz.

The current flowing through the coil is monitored using a current probe (A6303XL, Tektronix) and an oscilloscope (DSO81204B, Agilent). Magnetic fields were measured up to 4 kA/m using a magnetic field sensor (100B, Magnetic science). At magnetic fields of 4 kA/m or more, field intensity could not be measured owing to sensor overheating. Intensity was estimated using 3D electromagnetic simulation (CST Studio Suite 2009) and theoretical calculations based on magnetic vector potential [26, 27]. When current is applied to the coil, the conduction loss of copper causes undesirable heat. As this heat may affect the temperature of the MNC solution, cooling water flows in the pipe to suppress the temperature increase in the coil. The temperature of the MNC solution was measured using optical fiber thermometers (Luxtron m822, USA) because conductor thermometers can change the boundary conditions of the magnetic field. Fig. 10 shows the model used for the electromagnetic simulation, the simulated magnetic field, and the setup for the temperature measurement of the MNC with the manufactured coil and optical fiber probe.

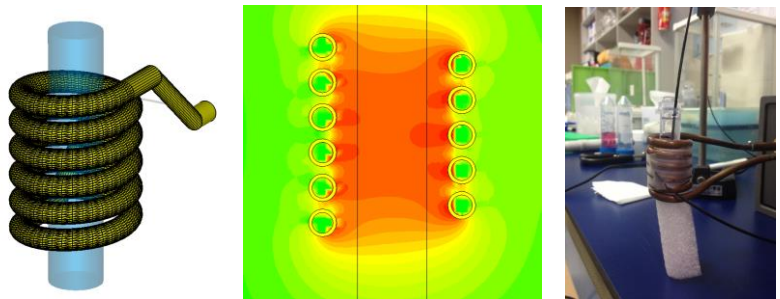


Fig. 10. (a) Solenoid coil model for 3D electromagnetic simulation. (b) Magnetic field distribution. (c) Experimental setup of the coil, MNC solution, and optical fiber probe.

## 2.4 SLP Measurement

The SLP of MNCs represents the heating efficiency and depends on the size of the particles, saturation magnetization ( $M_s$ ) and magnetic anisotropy of the MNC [29]. For a given iron oxide MNCs, the mean size of MNCs with applied AMF is an important parameter for optimizing SLP [16, 30]. We measured the temperature increase in the MNC solutions by changing the frequency and intensity of the magnetic field. SLP was calculated using the following equation [17]:

$$SLP = \frac{c_i m_i}{m_{Fe}} \frac{\Delta T}{\Delta t} \quad (8)$$

where  $c_i$  is the specific heat capacity of the medium,  $m_i$  is the mass of the medium,  $m_{Fe}$  is the mass of the MNC in the medium,  $T$  is absolute temperature,  $t$  is time, and  $\Delta T/\Delta t$  is the difference between the initial temperature and the temperature after 100s.

Fig. 11 shows the heat generation performance of the MNCs according to the change in field intensity and frequency. At 1.45 kA/m (black line), The SLP is not high at all frequencies and the difference of SLP according to the size of the MNCs is also very small. This is consistent with the fact that the coercivities are similar in Table II. As the magnetic field strength increases, there is a difference in the increase of SLP according to the size of the MNCs. In the case of 756 kHz and 1056 kHz, SLP increases to similar values for the 20 nm, 30 nm, and 40 nm MNCs when intensity increases from 1.45 kA/m to 3.95 kA/m; however, the increase for the 60 nm and 80 nm MNCs is small. At 756 kHz, as intensity increases to 6.45 kA/m, the SLP for the 60 nm MNC increases considerably to the highest value of 240 W/g.

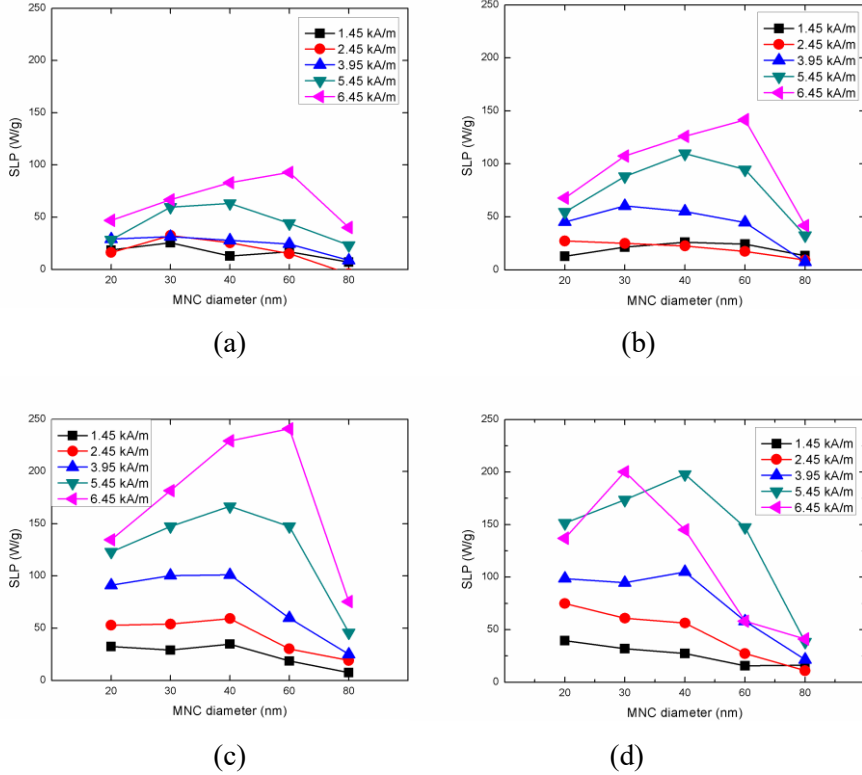


Fig. 11. SLP of MNCs. The frequencies are (a) 289, (b) 387, (c) 756, and (d) 1056 kHz.

The energy barrier of a single domain increases with particle size. As the crystal size for the 60 nm MNC (crystal size = 19.8 nm) is larger than that for the 40 nm MNC (crystal size = 9.9 nm), the intensity of the magnetic field required to cross the energy barrier for the 60 nm MNC is higher than that for the 40 nm MNC. The MNC with sufficient energy to cross the energy barrier can increase the area of the magnetic hysteresis loop. The highest SLP of the 60 nm MNC at 6.45 kA/m can be interpreted as the supply of magnetic energy beyond the energy barrier of the 60 nm MNC. The same phenomenon was expected in the case of 1056 kHz; however, there

was no significant increase in temperature owing to agglomeration in the solution at an intensity of 6.45 kA/m. It is considered that the aggregation reduced Brownian loss and strengthened the interaction between the MNCs. The effect of aggregation on heat generation in relation to the surface coating and concentration of nanoparticles must be further investigated. Except for the case where aggregation occurs, the 60 nm MNC with sufficient magnetic field strength (6.45 kA/m) exhibits the highest SLP at all frequencies.

If only the heating effect is considered, and not the purpose of cancer treatment, it is better to use high frequency and a strong magnetic field. A temperature between 42 °C and 50 °C should be maintained to treat cancer tissues with apoptosis. In addition, considering thermal tolerance and treatment time, the temperature of the tissues must be increased rapidly. When the MNCs are absorbed into living tissues, the Brownian motion is limited, and as a result, SLP is reduced. Moreover, it is difficult to predict the effect of biological factors on the heat generation mechanism of the MNCs. Therefore, by adjusting the intensity and/or frequency of the magnetic field, the temperature of cancer tissues should be rapidly increased to 42 °C. Then, the magnetic field must be adjusted such that a temperature between 42 °C and 50 °C is maintained for approximately 30 min[31]. This temperature range and period may vary depending on the experimental and biological environment.

Rosensweig proposed that the heating mechanism of magnetic nanoparticles in an alternating magnetic field depends on the conditions of the applied magnetic field and the properties of the particles [21]. He proposed the following equation, which expresses the heating power of relaxation loss:

$$P = \pi \mu_0 \chi_0 H_0^2 f \frac{2\pi f \tau}{1 + (2\pi f \tau)^2} \quad (9)$$

where  $P$  is the heat dissipation value,  $\mu_0$  is the permeability of vacuum,  $\chi_0$  is the initial magnetic susceptibility, and  $\tau$  is relaxation time.  $H_0$  and  $f$  are the intensity and frequency of the external magnetic field, respectively.  $P$  is proportional to field frequency and the square of strength. Hysteresis loss is expressed as the product of frequency and the area of the loop, and it is proportional to intensity [32]. The frequency limit in hyperthermia is owing to the occurrence of eddy current, which is expressed as the product of frequency and the magnetic field strength [33]. According to this theoretical background, controlling the heat generation of MNCs is advantageous for changing the intensity of the magnetic field. Therefore, we must select an efficient frequency to perform hyperthermia therapy. The energy conversion rate of the MNCs was calculated. Fig. 12 shows SLP divided by frequency. A sample of the 60 nm MNC at 387 kHz and 6.45 kA/m provided the highest efficiency. This magnetic field condition has a lower risk of eddy current occurrence than the case of 756 kHz and 6.45 kA/m. In this study, we selected the 60 nm MNC with a magnetic field of 387 kHz to treat tumor tissues. The strength of the magnetic field was increased until the temperature of the tumor tissues reached 42 °C.

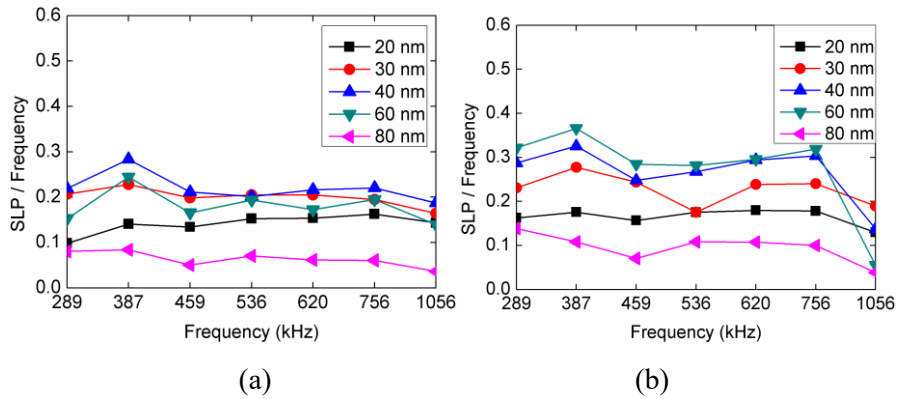


Fig. 12. SLP per unit frequency. The field strengths are (a) 5.45 kA/m and (b) 6.45 kA/m.

## 2.5 Cancer Cell Experiments

The breast cancer stem cells (bCSCs) were prepared in accordance with the method of Dontu *et al.* with modifications [34]. The human breast cancer cell line BT-474 was obtained from the American Type Culture Collection (ATCC). Cells were grown as monolayer, routinely cultured in Hybri-Care Medium (ATCC), and maintained in MEM medium (GIBCO, Invitrogen) supplemented with 10 % FBS (GIBCO, Invitrogen), 10 µg/mL insulin (Sigma), and penicillin/streptomycin (GIBCO, Invitrogen). For mammosphere culture, cells were suspended at a density of 50,000 cells/mL and seeded into 6-well plates (2.5 mL/well) in DMEM/F12 (1:1) media containing 5 µg/mL bovine insulin (Sigma), 0.4 % bovine serum albumin (Sigma), 2 % B-27 supplement (Invitrogen), 20 ng/mL basic fibroblast growth factor (Preprotech), and 10 ng/mL epidermal growth factor (Sigma). One milliliter of fresh media was added to each well every 2 days (without removing the old media). Mammospheres were collected on day 9 by gentle centrifugation and were dissociated to single cell suspensions by treatment with 0.05 % trypsin-EDTA for 10 min. For mammosphere formation, the single cells (1,000 cells/mL) were cultured in suspension (60 mm-petri dish flask) to generate mammospheres of the next generation. The percentage and size of the wells with mammospheres were analyzed at the indicated times. For each passage cultured cells, ALDH1 expression was determined with the ALDEFLUORTM fluorescent reagent system (Stem Cell Technology, Canada), to identify cells expressing ALDH1 activity as a biomarker for bCSCs by using flow cytometry (BD Biosciences)[35]. For the detection of CD44+/CD24-, cells were stained in 96-well plates in a volume of 50 µL, with 2 µL of each monoclonal antibody per well: CD24-Alexa648, CD44-FITC, and ESA-

PcPCy5 (BD Biosciences). Isotype-matched labeled controls were also used in the analysis. Cells were labeled on ice for 30 min and washed twice before analysis with a cytometer.

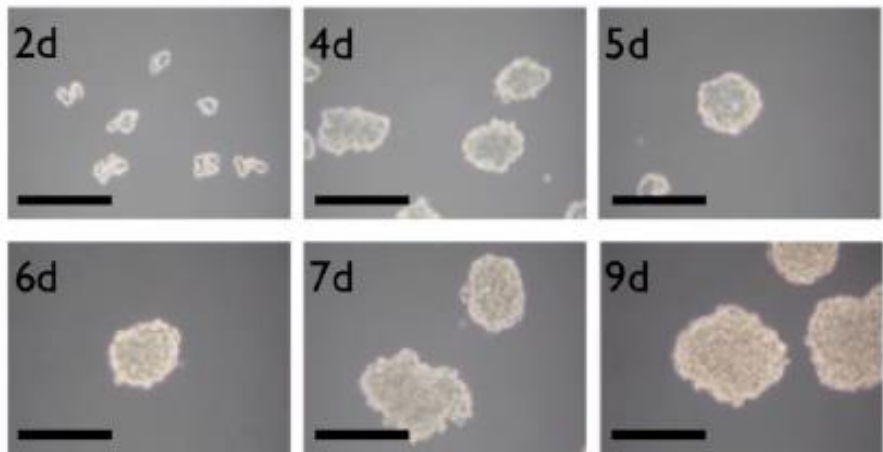


Fig. 13. Characterization of mammosphere (MS) formation.

The mammosphere (MS) diameters were determined with an inverted microscope using the Image J software according to the typical CSC characterization method. Fig. 13 shows formation of MS.

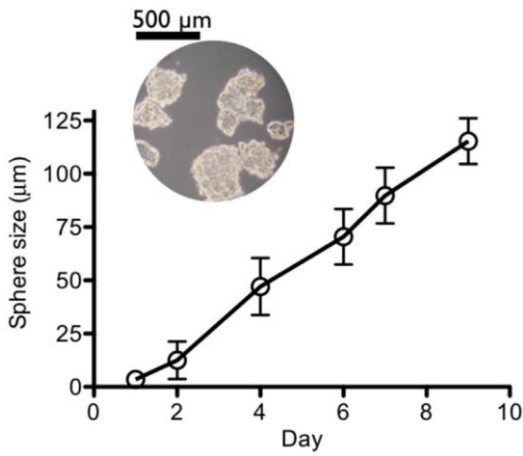


Fig. 14. MS formation. The size of the cultured MS at different days.

As shown in Fig. 14, the whole size of the cells gradually increased from a single cell (~20 mm) to the MS form (~120 mm) in the culture media.

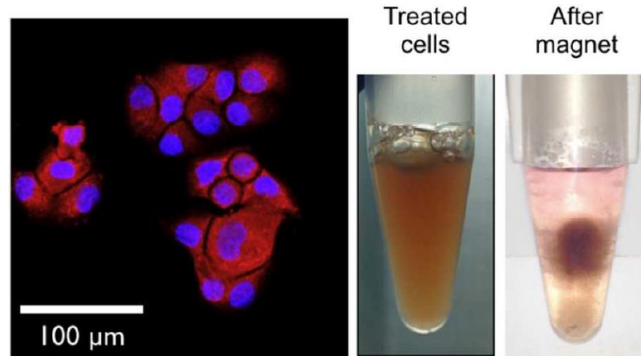


Fig. 15. Confocal microscopic image of the MS cells treated with red fluorescent MNC particles and the floating cells after MNC treatment.

The red fluorescent MNC particles were prepared by RITC and EDC/NHS conjugation method, and the bCSCs were treated with these particles for 3 h, followed by washing three times with culture media to eliminate excess particles. As

in Fig. 15, the fluorescence intensity was determined with a confocal microscope and showed that the particles could penetrate into the cell cytosol. The treated cells were responsible for the external point magnet owing to the magnetic property of the internalized MNCs.

From the results of the SLP measurement, 60 nm sized MNCs were used for thermal therapy to target bCSCs. The concentration of MNC absorbed in the prepared CSC was very low. CSCs that absorb these low concentrations of MNCs require strong magnetic fields for hyperthermia treatment. When the inverter system for SLP measurement was used, the temperature of the CSCs did not exceed 42°C, so we used commercial equipment (EasyHeat 0224, Ambrell). EasyHeat was able to generate a magnetic field of 60 kA/m at 290 kHz, thus ensuring a sufficient temperature. To compare the magnetic hyperthermia effect, bCSCs were treated with the 30 nm and 60 nm sized MNCs (0.2 mg/mL) for 3 h at 37°C in a CO<sub>2</sub> incubator and the excess particles were removed by washing gently several times with a PBS buffer solution. Then, the cells were treated with trypsin–EDTA solution to detach cells.

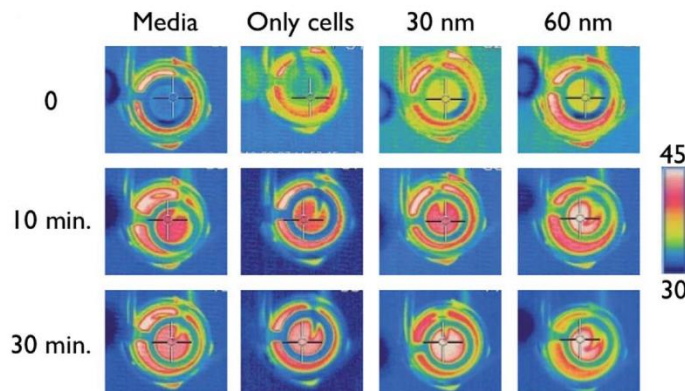


Fig. 16. Images from the infrared camera during AMF application at different times (heat scale unit: °C).

The cells were exposed to a magnetic field after homogeneous mixing with an agarose solution for different durations. Fig. 16 shows thermal images of solenoid coil and MNC sample. The media and only cell samples (untreated) acted as controls and exhibited a similar temperature increase ( $40^{\circ}\text{C}$ ). The temperature increase was caused by the warming of the magnetic coil during the application of the external field. These results indicated that the cell without MNCs sample did not affect the hyperthermia initiated by the external magnetic field. The MNCs-treated cells showed a higher increase in temperature than the controls.

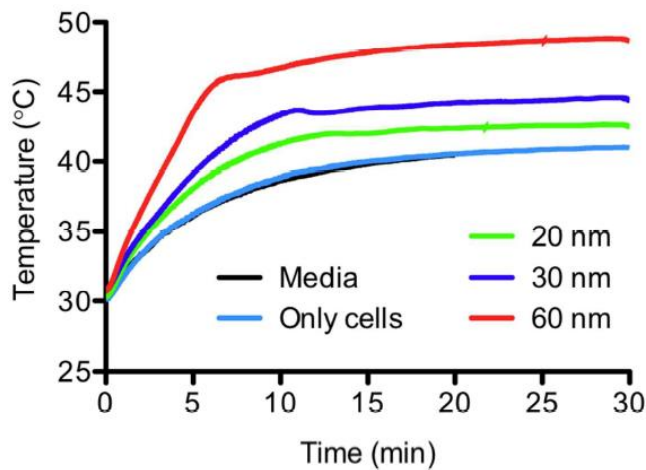


Fig. 17. Temperatures generated by the MNCs of various sizes, media, and cell only (untreated) samples at different times.

Fig. 17 is a graph of the temperature change of the sample over time. Similar with the SLP results, cells treated with the 60 nm MNCs demonstrated the highest and fastest increase in temperature ( $47^{\circ}\text{C}$ ) within 10 min. From these results, the 60 nm MNC particles appear to be an appropriate magnetic material size for thermal therapy because the heating of cells to temperatures between  $42^{\circ}\text{C}$  and  $46^{\circ}\text{C}$  resulted

in the death of tumor cells. Above this temperature, healthy cells could be affected to induce necrosis.

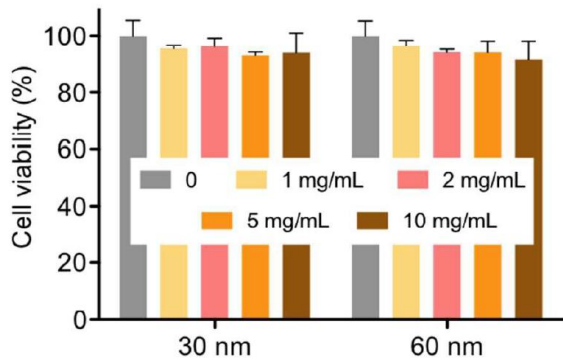


Fig. 18. Cell viability at different concentrations of the MNCs in the absence of an AMF.

The cell viability was determined by the WST-1 assay after MNCs treatment. Both the 30 and 60 nm sized MNCs did not exert acute cytotoxicity with various concentrations of the particle solutions in the absence of a magnetic field as shown in Fig. 18.

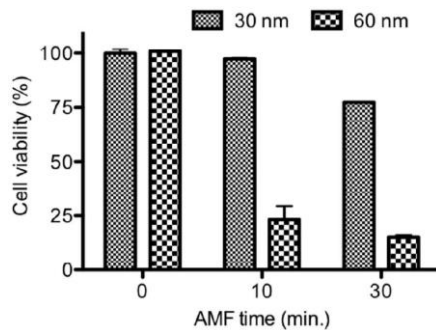


Fig. 19. Cell viability at different treatment times of AMF.

In Fig. 19, under the AMF conditions, the 60 nm MNC dramatically reduced cell viability within 10 min, while the 30 nm MNCs did not significantly decrease cell viability, possibly because the produced temperature (43 °C) was not enough to induce cell death. This was consistent with the results observed with the hyperthermia experiments in the tube. At this point, we suggest that magnetic hyperthermia for cancer therapy could induce cell death at temperatures over 43°C.

## 2.6 Mouse Experiments

The complex effects of blood perfusion, cancer cell growth, and metabolism alter the heat-generating conditions of nanoparticles, which cannot ensure the effect of MNCs as a hyperthermia treatment. Therefore, it is necessary to check the effect through *in vivo* tests.

*In vivo* experiments were performed with xenograft mice to confirm the efficacy of the MNC as a cancer treatment. Seven BALB/c nude mice were used for the xenograft. Female BALB/c nude mice (5 weeks old, Charles River, Wilmington, MA, USA) were used to prepare the tumor-xenografted mouse model. The mice were kept in a light-controlled room maintained at a temperature of  $22 \pm 2$  °C with a relative humidity of  $55 \pm 5\%$  (Animal Center for Pharmaceutical Research, College of Pharmacy, Seoul National University, Korea). We changed the cage every day and checked the condition of the mice. The experimental protocols for the animal study were approved by the Animal Care and Use Committee of the College of Pharmacy, Seoul National University. Squamous cell carcinoma 7 (SCC VII, Korean Cell Line Bank) was implanted as a cancer cell line. The mice injected with cancer cells did not show signs of activity change or disease during their survival. All mice were euthanized at different times during the experiment depending on the size and condition of the cancer.

The mice were divided into four groups. The first sham group was exposed to the magnetic field without MNC injection. The tumor size of the control group was measured for 3 weeks. The treatment group was measured 18 times in 4 weeks. The growth rate of the treatment group did not differ from that of the control group. Rectal temperature did not change when the leg where the tumor tissue was located

was exposed to the magnetic field. It can be determined that the induced current generated by the magnetic field is not sufficient to increase body temperature. The second sham-treatment group contained cancer cells with the MNC, and magnetic field exposure was excluded.

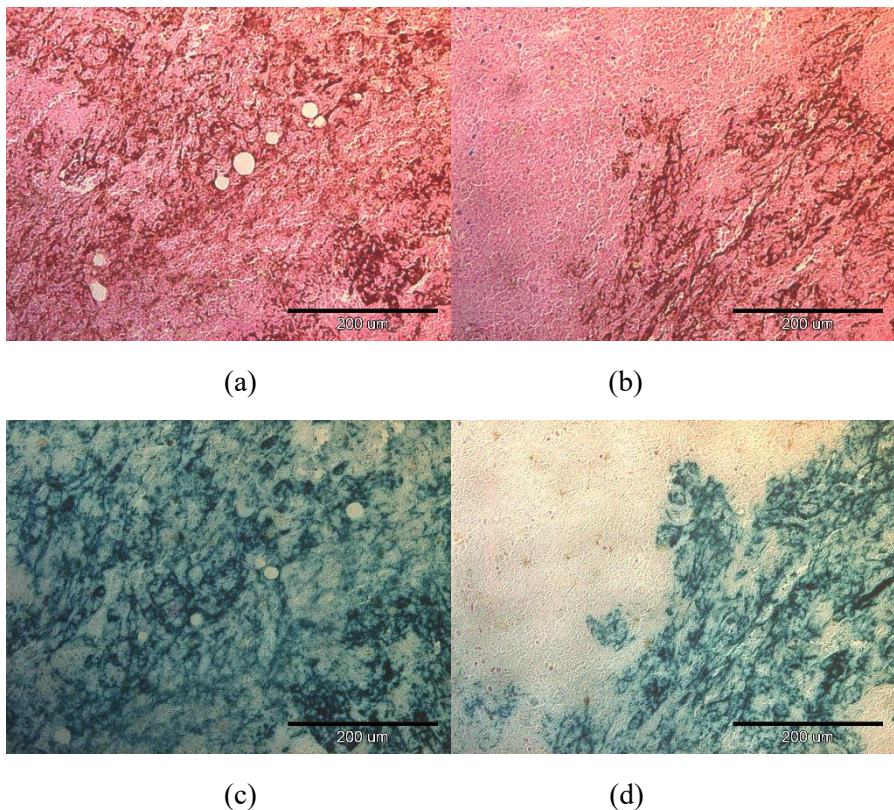


Fig. 20. Microphotographs of the cancer: (a) and (b) Hematoxylin and eosin (HE) staining, (c) and (d) Prussian blue staining.

One of the mice in the second sham group was sacrificed through euthanasia using carbon dioxide (CO). One hour after MNC injection, the extracted tumor was stained with Prussian blue to identify the homogeneity of the MNC within the tumor tissues.

In addition, hematoxylin and eosin staining was applied for verification. Fig. 20 (a) and 20 (c) show microscopic photographs of the tumor tissues. The MNC is relatively uniformly distributed in the area directly injected through a syringe (Hamilton 81156, Thermal scientific, INC). However, the MNC did not spread throughout the tumor tissues. Fig. 20 (b) and 20 (d) show the boundary between the absorbed and non-absorbed MNC.

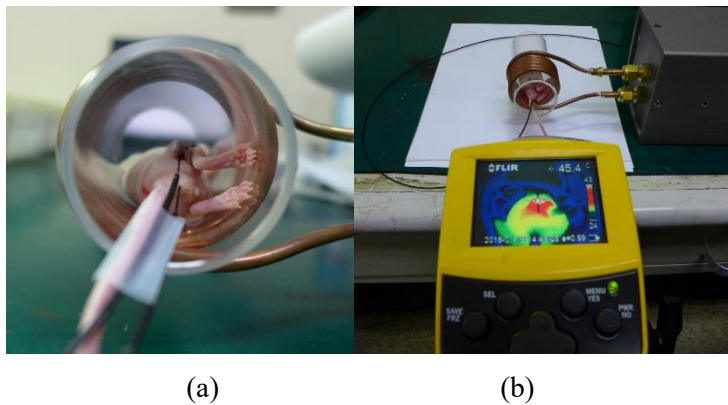


Fig. 21. Experimental settings: (a) The mouse lay inside the jig. The cancer tissue is at the center of jig. (b) The IR camera measures the skin temperature of the mouse.

The treatment group was anesthetized by intravenous injection of ketamine. After anesthesia, the solution of MNCs was directly injected into tumor region over 10 minutes using the Hamilton syringe. At the time of injection, the size of the tumor was  $5.09\text{ mm} \times 6.83\text{ mm}$ . 0.04 ml of magnetic fluid having a concentration of 40 mg/ml was injected into the center of the cancer tissue. The injected MNC was exposed to a magnetic field after one hour to be accumulated in the cancer cells. After the injection of the solution, the animal was placed in a plastic jig that does not

interfere the magnetic field distribution. The jig is located inside the coil with an inner diameter of 40 mm. The solenoid coil is larger in diameter than the SLP measurement, and the cancer tissue in the mouse's leg is located at the center of the coil. To generate heat, cancer with MNC was exposed to a magnetic field of 387 kHz. The temperature of tumor tissue was measured by using optical fiber thermometer and an infrared (IR) camera (E25, FLIR). Fig. 21 shows the experiment settings. The fiber probes are inserted into the rectum and cancer tissues, respectively, and the IR camera measures the skin temperature of the mouse.

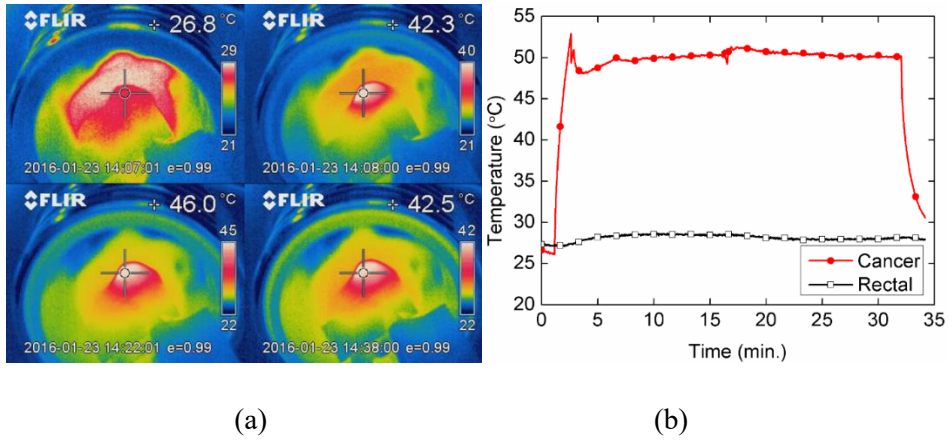


Fig. 22. (a) Photographs of the IR camera, (b) the optical fiber thermometer results.  
(The symbols in the graph do not represent measurement points.)

The intensity of the magnetic field was adjusted (between 8.25 kA/m and 9.9 kA/m) so that the temperature of the treatment region remained between 45°C and 50°C. In previous cell experiments, apoptosis was observed between 45 ° C and 50 ° C, so the in vivo experiment maintained a higher temperature range than the temperature range used in conventional hyperthermia [17]. The magnetic field was maintained for 30

minutes [31]. Fig. 22 (a) shows the skin temperature taken with an IR camera increased from  $26.8^{\circ}\text{C}$  to  $42.3^{\circ}\text{C}$  in one minute. The maximum temperature of the skin was  $46.0^{\circ}\text{C}$ , and the experiment was stopped at a skin temperature of  $42.5^{\circ}\text{C}$ . Obviously, the point where the MNC was injected was higher than the skin temperature. In Fig. 22 (b), the initial temperature rise of the MNC was very steep and after  $50^{\circ}\text{C}$ , the magnetic field strength was adjusted to maintain the under  $50^{\circ}\text{C}$ .

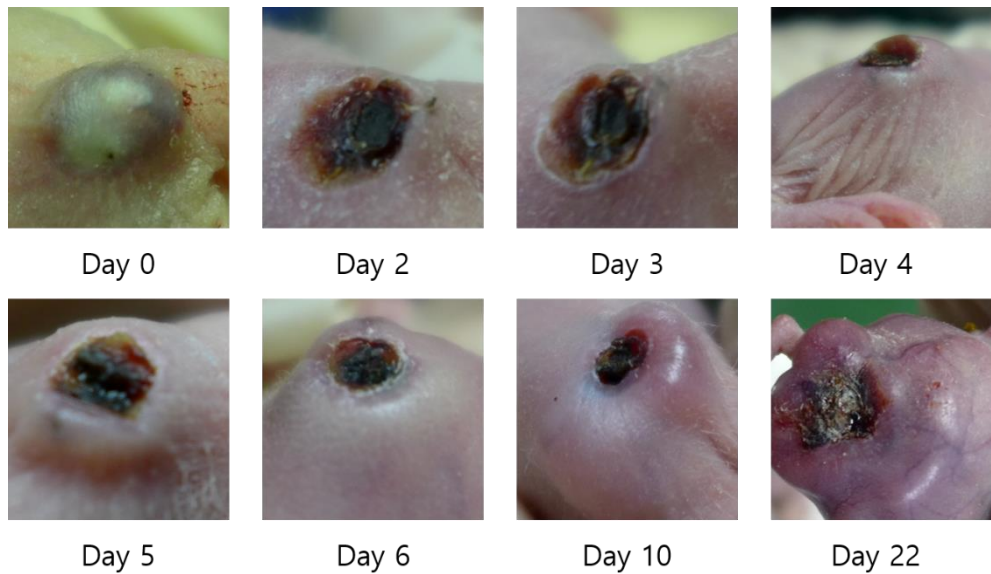


Fig. 23. Photographs of cancer tissue of nude mice.

Fig. 23 shows a photograph of the cancer after hyperthermia treatment. The cancer tissue became black due to the injection of MNC and turned white immediately after the treatment of hyperthermia. Two days later, the thickness of the cancer tissue decreased considerably and changed to black. Three days after, it turned like a scab, and the treatment effect was expected. However, after four days, Cancerous tissues below the skin and around the MNC implanted area have grown rapidly. As a result,

MNC seemed to remove some cancer tissues, but the remaining cancer cells continue to multiply, making it difficult to be sure of the therapeutic effect.

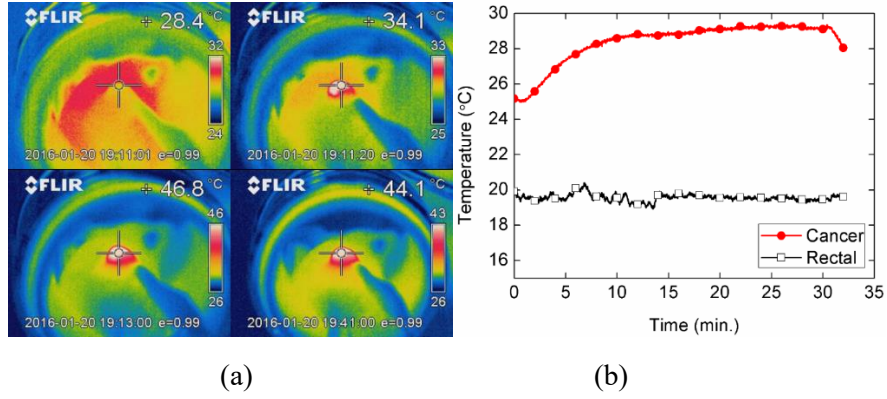


Fig. 24. (a) Photographs of IR camera, (b) the fiber optic thermometer results. (The symbols in the graph do not represent measurement points.)

The MFH therapy was repeated in two other mice (no. 6 and 7) with different MNC injection method. The MNC was directly injected into the cancer tissue of similar size as the previous test. In this trial, three or four injections were made to distribute evenly, near the border between cancer and normal tissue. At the time of injection, the size of the tumor was 7.3 mm × 5.2 mm and 6.76 mm × 5.38 mm, respectively. The infrared camera measured the skin temperature as before. The optical fiber probe was inserted into normal tissues close to cancer tissues and temperature was measured. This probe is to observe whether the temperature of normal tissues goes up. Another probe is inserted into the rectal. The skin temperature increased from 28.4°C to 46.8°C in 2 minutes. The magnetic field was then adjusted to maintain the temperature at about 45°C. Fig. 24 (a) is a photograph taken with an IR camera. The treated area shows a high temperature in red or white,

and the temperature of the other parts does not rise. In the result of optical fiber probe in Fig. 24 (b), the rectal temperature remained constant, indicating that the body temperature of the mice was not affected. The normal tissue near the cancer was assumed to be undamaged because another probe would rise by about  $4^{\circ}\text{C}$  and not exceed  $30^{\circ}\text{C}$ .

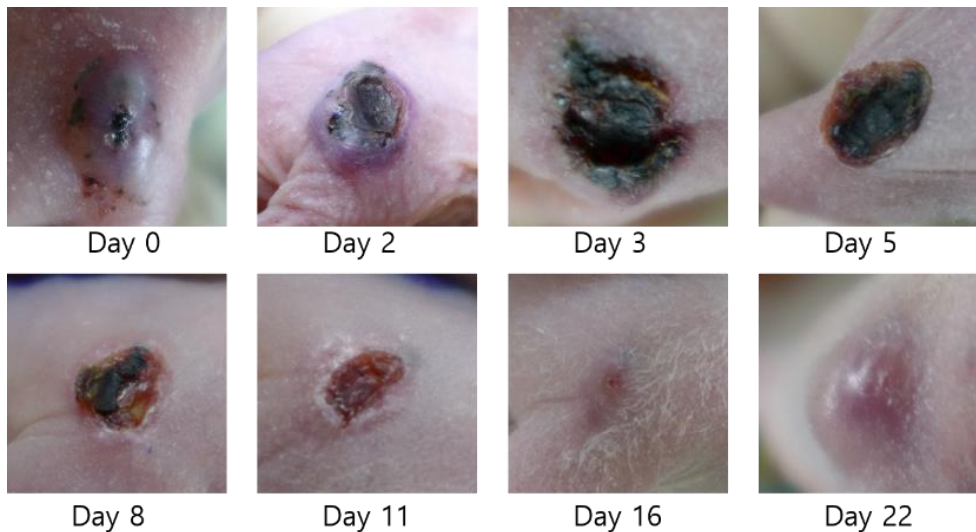


Fig. 25. Photographs of the tumor treated with MFH.

Fig. 25 shows a photograph of the change of the cancer over time. Immediately after the treatment, it seems that there is no change on the normal tissues. Two days later, second MFH was performed because the cancer tissue still remained untreated. In the photo of Day 2, a second treated area is seen around the scab. On Day 3 all the exposed area had scab. On Day 5, normal skin and scab boundaries became clear. On Day 16, it was confirmed that all of the external injuries were treated. After 20 days of the first treatment, cancer recurred.

Another mouse in the treatment group (no. 7) showed similar results to the no. 6. After the hyperthermia treatment, the destruction of the cancer confirmed. But recurred after 13 days. When the hyperthermia conducted the volumes of treated cancer were  $98.7 \text{ mm}^3$  and  $97.83 \text{ mm}^3$  and the sham control was  $110.37 \text{ mm}^3$ . The volume of tumor was determined by the following relationship [36]

$$\text{volume} = \text{length} \times \text{width} \times \frac{\text{width}}{2} \quad (10).$$

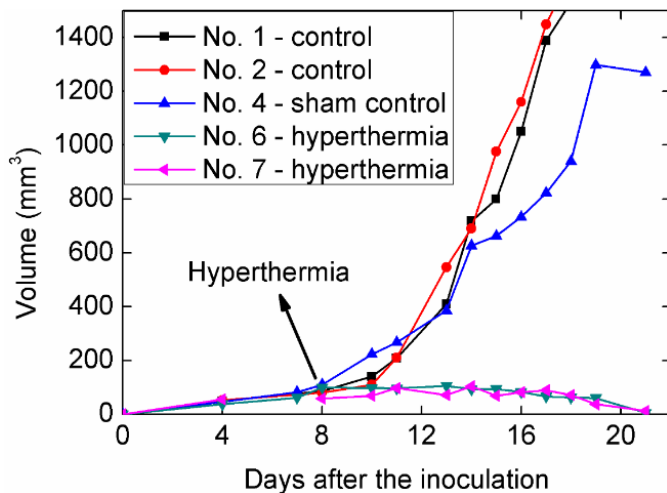


Fig. 26. The cancer volumes for control, sham-treated, MFH treated group were plotted as a function of time.

The cancer volumes were plotted as a function of time in Fig. 26. All cancer showed similar growth rates until MFH treatment. Hyperthermia therapy was performed on the eighth day after cancer inoculation. The cancer tissues of mice treated with hyperthermia were observed to decrease in size. In contrast, sham-treated mouse and control group grew over  $500 \text{ mm}^3$  after two weeks.

# **Chapter 3 Brain Stimulation**

## **3.1 Introduction**

Diverse brain stimulation techniques have been used to modulate brain activities during clinical and basic researches [37-40]. Especially, brain stimulation methods using electrical and magnetic components have grown over the past decades and their effect on neural circuits and behaviors have been intensively investigated [40-43].

Conventionally there are several different ways to stimulate the brain. Deep brain stimulation (DBS), for example, is an invasive stimulation method where electric current is passed through electrodes at specific parts of the brain for neuromodulation. Transcranial magnetic stimulation (TMS) [43-46] and transcranial direct current stimulation (tDCS) [47, 48], on the other hand, are typical noninvasive brain stimulation methods. tDCS utilizes electric current (usually  $0.029 \text{ mA/cm}^2$ ) flows between the two electrodes attached to the scalp to induce electrical potentials to stimulate neurons in the brain [48], while TMS uses electric currents induced by alternating magnetic field to stimulate the brain [43-46]. Repetitive TMS (rTMS) were shown to safely modulate human brain activity [45] and the frequency of repetitive magnetic field played a key role in modulating the excitability in the cerebral cortex [46].

There are pros and cons to the conventional noninvasive brain stimulation methods. tDCS is less expensive than TMS [49, 50], but it is a relatively primitive technique compared to TMS. It is inefficient because approximately half of the DC current flows out through the scalp [51], it has difficulty in focusing the stimulation location,

and it causes more skin irritation than TMS. Despite the advantage that TMS has over tDCS, TMS also has disadvantages in high cost, lack of portability, and disturbing acoustic noise [50]. In addition, TMS needs further improvement in the energy needed for stimulation and specificity of stimulation location. The induced current for stimulation requires a magnetic field of several tesla (T), which requires high power consumption. Figure 8 coils used in TMS to focus stimulating effects to a small area could also form a considerable magnetic field around the wing of the coil, thereby unintentionally activating non-target areas [52].

Evidences show that the electromagnetic field directly affects the biological system, such as temperature rise, molecular signaling, and interaction with the neurons [53]. Recently, new brain stimulation techniques have been developed to more efficiently treat neurological and psychiatric disorders [54, 55]. In another paper, changes in the amplitude of microwave signals were reported to induce changes in brain activity [56, 57]. In this dissertation, new brain stimulation method was designed by combining above two concepts. The proposed system modulates a continuous wave (CW) signal into a pulse envelope signal. Because the neuron has low-pass filter characteristics, the modulated signal will be able to induce a change in the activity of the neuron.[58].

This chapter consists of two major parts. The first is a brain stimulation system for small animals that combines pulse envelope modulation with a conventional magnetic stimulation system. The second is a brain stimulation system that is made by pulse-modulated microwave signal.

### **3.2 Transcranial Magnetic Stimulation**

A typical noninvasive brain stimulation method is a transcranial magnetic stimulation (TMS). TMS uses electromagnetic induction as a highly effective painless way to generate threshold current in the brain. The AMF can induce an electric field and thus form an induced current in the brain. A conventional TMS device consists of a copper wire connected to the terminals of a large electrical capacitance via a switch. The capacitance is discharged by closing the switch so that a large current of several thousand amperes flows transiently through the wire coil for a period of less than 1 msec. If the coil is placed on the head of a subject, the magnetic fields strengths up to several tesla readily penetrate into the brain without attenuation by the scalp or skull and generate a current according to the Faraday's law [26, 27] of electromagnetic induction. If the magnetic field strength is sufficient, the induced current can depolarize superficial axons and activate neural networks in the cortex. The range of the current density generated in the brain depends on many physical and biological parameters, such as the type and orientation of stimulus coil, the distance between the coil and the brain, the magnetic pulse waveform, the intensity, frequency and pattern. This chapter consists of a newly proposed signal generation system for TMS and animal experiments using it.

### **3.2.1 Pulse envelope modulated AMF generation system**

This section describes a magnetic field generator capable of stimulate the brain of small animal such as mice. A high intensity magnetic field is needed to induce current in the brain. Fig. 27 shows typical TMS system and the newly proposed pulse envelope TMS system. In conventional TMS system configuration, the switch only can be turned off when the coil current becomes zero. In this configuration, the pulse width is only determined by the resonant frequency which is the inverse of the capacitance of the charging/discharging capacitor multiplied by the inductance of stimulus coil. The existing TMS devices can adjust the resonant frequency in a limited way, such as changing the capacitance or inductance. Therefore, a pulse width control is difficult. To control the frequency and intensity of the magnetic field, the same AMF generation system used for MFH was used. The proposed AMF generator for brain stimulation could control the envelope of the CW signal using a full-bridge inverter. A detailed description of the inverter operation is given in section 2.3.2. By adjusting the sequence of the switches, the envelope of the output ac signal can be made as shown in Fig. 27. In this experiment, a control signal was generated using a data generator (DTG5274, Tektronix). In a pulse period where the pulse envelope is needed, the normal switch sequence is transmitted to the driver amplifier. During a rest period, all switches were turned off. As a result, the output signal of the inverter was made to be a pulse envelope. The brain stimulation signal generated in this way is very free to adjust the pulse width. In Chapter 3, the CW signal was modulated using a switch rather than a data generator.

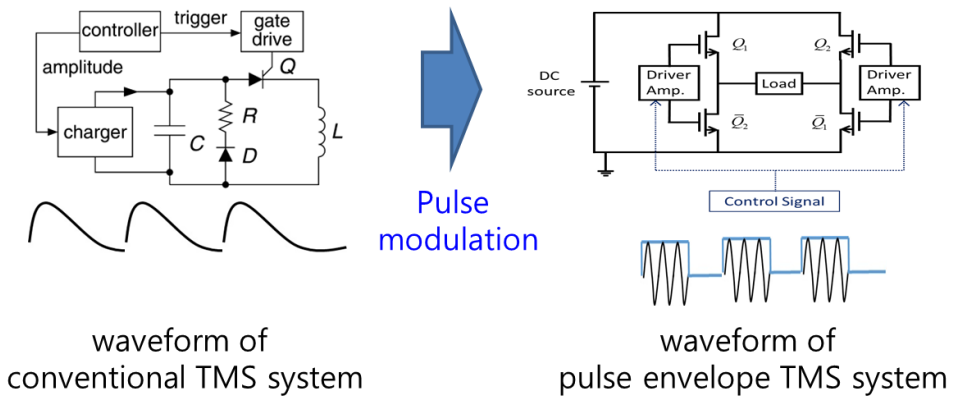


Fig. 27. The existing TMS system and the newly proposed pulse envelope TMS system.

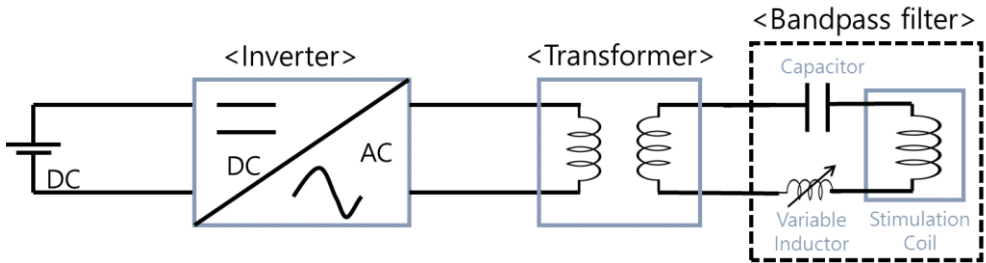


Fig. 28. Block diagram of proposed TMS system.

The proposed TMS system configuration is shown in Fig. 28, which includes a full-bridge inverter, transformer, series LC resonant circuit, and a variable inductor. The insertion loss is the smallest when the center frequency of the band-pass filter matches the output frequency of the inverter. In MFH, fine tuning was not required because the characteristics of the nanoparticles did not change significantly with small changes of the AMF frequency. However, the effect of the AMF frequency changes on neurons has not been studied. Therefore, the resonance frequency of the filter needs to be fine-tuned when the frequency of the inverter output signal changes little by little. When attempting to change the resonant frequency of filter, the

capacitance and inductance of the filter must be changed. At this time, it is important that the magnetic field strength of the stimulus coil causing the brain stimulation is kept constant. In this study, resonant frequency was changed by attaching variable inductor.

In the conventional repetitive TMS (rTMS), the stimulation effect of the brain varies according to the repetition period of the pulse. Neurons exhibit frequency response characteristics similar to those of low-pass filters[54, 58], responding to low-frequency signals without reacting to high-frequency signals. Taking this into consideration, the neuron will be able to respond to the stimulation information if the high-frequency signal is modulated and the stimulation information is sent in envelope.

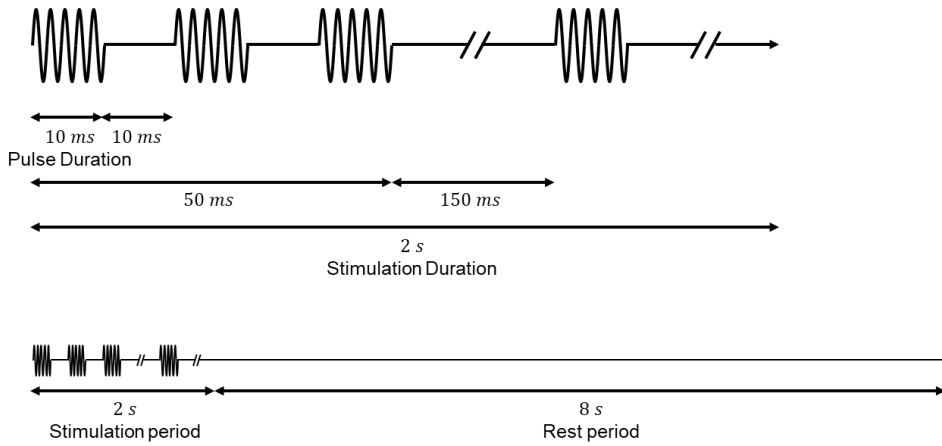


Fig. 29. The waveform of the proposed stimulation system.

Theta burst stimulation (TBS) is one of several pattern of rTMS [59]. TBS protocols have a major advantage over standard rTMS approaches in their reduced administration duration. The standard theta burst pattern consists of three bursts of

pulses given at 50 Hz and repeated every 200 ms. The inverter system was used to generate the signals of these complex protocols. The envelope of the inverter output signal was made into bursts of pulse shape of TBS. The current waveform at the output port of the proposed system is shown in Fig. 29.

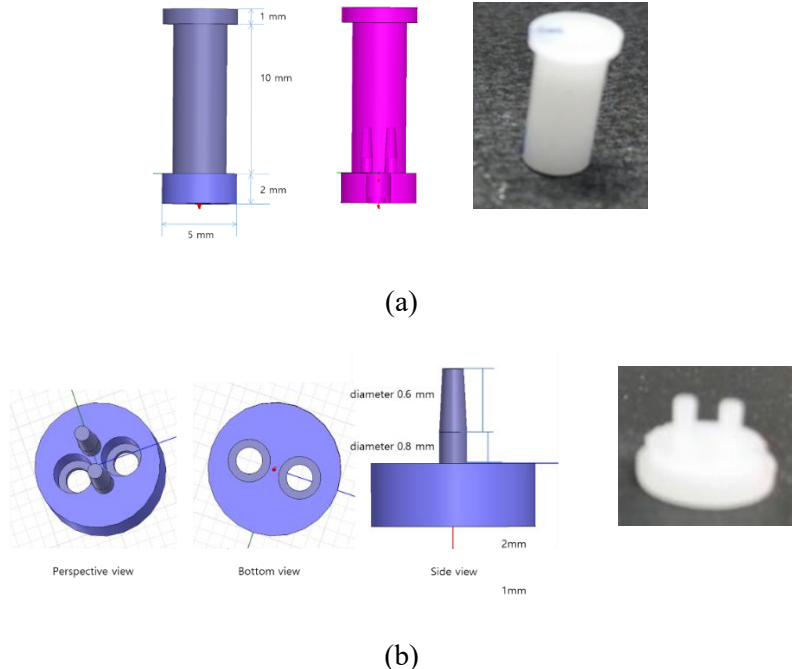


Fig. 30. (a) Upper pillar and (b) lower plate of the supporting stand.

The electric current which passes through the stimulus coil generates the magnetic field. Since the magnetic field has amplitude and direction, we need to design a stimulus coil to get a possible maximum amplitude and uniform direction in the brain. The simplest coil geometry satisfying the above condition is the solenoid. The weight and size of the coil were kept to a minimum so that the mouse are less stressed. In order to stimulate the fixed position, a supporting stand capable of fixing the coil

was used. The supporting stand can be divided into a lower plate and an upper pillar as shown in Fig. . The lower plate was fixed with cement to the mouse brain. The supporting stand was made of plastic materials that do not affect the magnetic field, thus satisfying both light weight and field distribution.



Fig. 31. Fabricated stimulus coil

The dimension of the solenoid coil is  $4 \times 10$  mm (diameter  $\times$  height). Enamel-coated insulated wires were used to prevent shorts when the coils were stacked, and the coil was wound 105 times to obtain the sufficient inductance and magnetic field intensity. Fig. 31 show a fabricated stimulus coil.



Fig. 32. Mouse with lower plate of supporting stand (left) and stimulation coil.

The weight of the support stand and solenoid coil were about 3 g. Fig. 32 shows the mouse with the lower plate implanted and full support stand with solenoid coil fixed to the mouse.

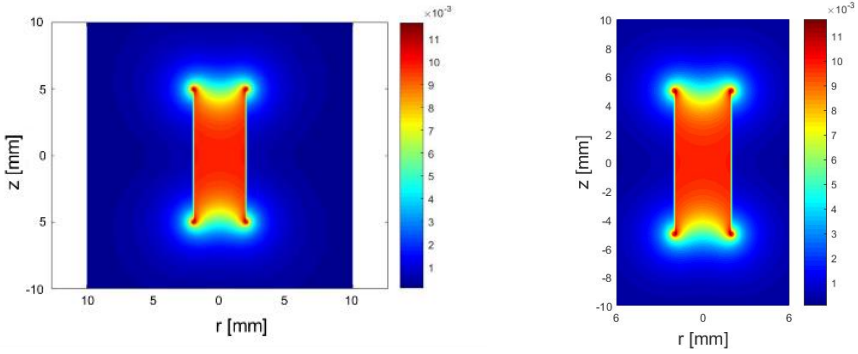


Fig. 33. Magnetic field distribution of the solenoid (side view).

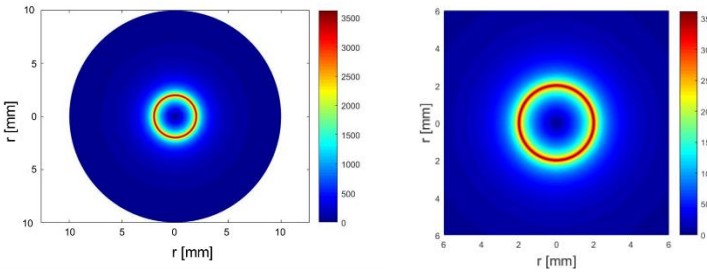


Fig. 34. Electric field distribution of the solenoid (top view, at  $z = 5$  mm).

Fig. 33 shows magnetic field distribution around the solenoid. Fig. 34. shows electric field distribution at the end of the solenoid, where  $z = 5$  mm, from the top view. Electric field becomes maximum at  $r = 2$  mm, the solenoid radius.

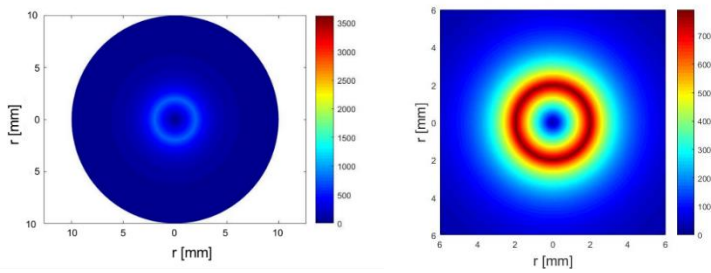


Fig. 35. Electric field distribution of the solenoid (top view, at  $z = 7$  mm).

Fig. 35 shows electric field distribution 2 mm away from the solenoid in the  $z$ -direction.

### 3.2.2 Mouse Experiment

TMS experiments employed first generation 129/SvJae X C57BL/6J hybride mice (male, 8-12 weeks). Mice were group-housed and maintained at 12 h light-dark cycle (lights on at 8 a.m.) with free access to food and water. Following a surgery, animals were singly-housed. All experiments were conducted in compliance with the Animal Care and Use Committee (Approval number: AP, 2015025). Mice were randomly assigned to experimental groups.

All surgical procedures were performed under anesthesia (30 mg/kg Zoletil, IP) and using a stereotaxic instrument (Kopf Instruments) with brain coordinates based on the mouse brain atlas [60]. Animals were given Ketoprofen (5 mg/kg SC) right after surgery and daily for a week for post-operative recovery.

For TMS, a plastic base plate was permanently affixed to the skull with Loctite 454 and dental cement. Later, a solenoid coil was connected to the baseplate for magnetic stimulation centering on the S1HL (AP: -0.5 mm, ML: -1.6 mm).

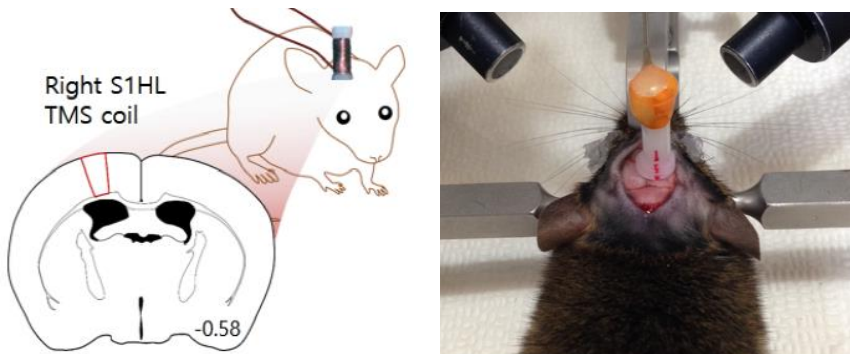


Fig. 36. Schematic drawing of TMS coil placement.

rTMS can have a cell type-specific effect in mice[61, 62]. In particular, intermittent TBS (iTBS), but not continuous TBS (cTBS), was shown to inhibit the

activity of parvalbumin interneurons in the various cortical areas including the somatosensory cortex. Thus, we secured a customized miniature TMS coil (Fig. ) above the right hemisphere to apply magnetic stimulation. TMS protocols used were, iTBS and cTBS, adapted from Haung et al. [59], and ‘Thalamic burst’, a new stimulation protocol devised based on thalamic burst firing patterns. For iTBS, 3 pulses at 50 Hz were repeated every 200 ms for 2 s with 8 s pause between bursts (Fig. 37). For cTBS, 3 pulses at 50 Hz were repeated every 200 ms for 40 s with a 160 s pause between stimulations. For ‘Thalamic burst’, 5 pulses at 333 Hz (3 ms between pulses) were repeated every 314 ms for 37.44 s with a 162.56 s pause between stimulations. Equal number of pulses were delivered for iTBS, cTBS, and ‘Thalamic burst’: a total of 4200 pulses were delivered during the 25 min stimulation time in von Frey tests and a total of 6000 pulses were delivered during the 35 min stimulation time in plantar and formalin tests. Pulse duration was 10 ms for iTBS and CTBS, while pulse duration for ‘Thalamic burst’ was 2 ms, due to a short interval between stimulation pulses.

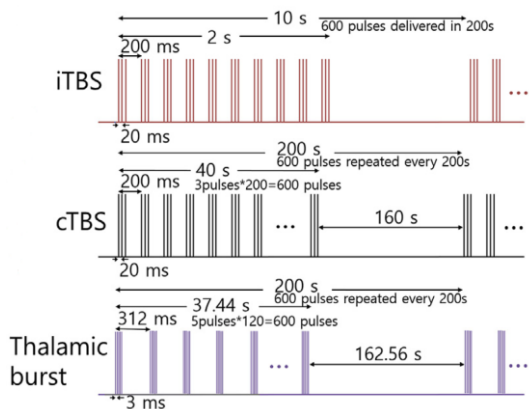


Fig. 37. The total numbers of iTBS, cTBS, and thalamic burst pulses were matched for each behavioral test (600 pulses/cycle, 1 cycle=3 min 20 s). Figure not drawn to

scale.

Since thalamic burst firings reduced nociceptive behavior by affecting the activity of cortical inhibitory interneurons, we tested whether TMS protocol mimicking thalamic bursts, ‘Thalamic burst’, could also reduce nociceptive behaviors. To test this, the ability of a newly developed ‘Thalamic burst’ protocol to modulate nociceptive behaviors were compared with those of established protocols, iTBS and cTBS. Nociceptive thresholds were measured before and after delivering identical number of pulses to keep the total number of stimulating pulses equal among stimulation protocols (see methods for details). ‘Thalamic burst’, iTBS, or cTBS was applied to separate groups of animals to assess whether non-invasive method could actually modulate nociceptive behaviors.

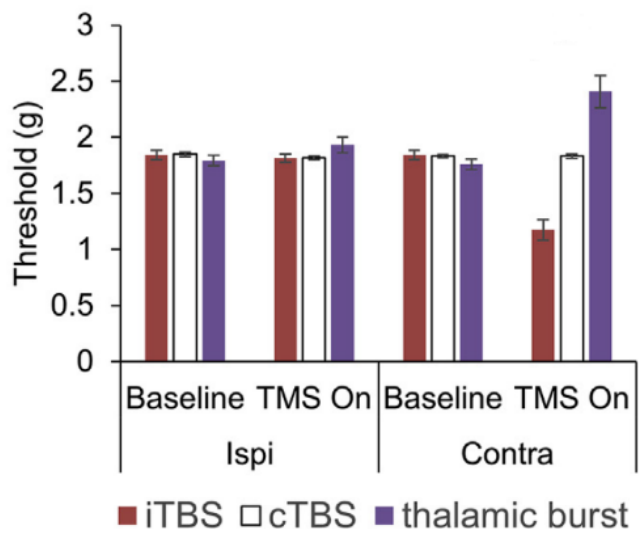


Fig. 38. Mechanical threshold changes induced by different TMS protocols. Paw withdrawal thresholds were measure with von Frey filaments (Kruskal-Wallis test with Mann-Whitney U test; n = 6 mice per group).

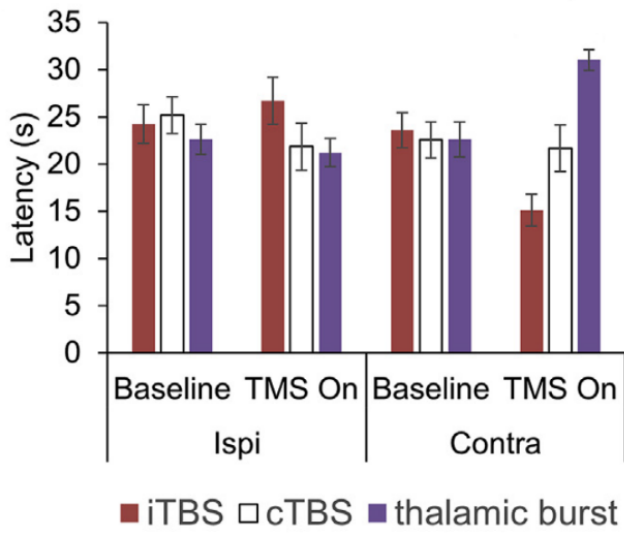


Fig. 39. Acute thermal nociception changes triggered by TMS protocols. Paw withdrawal latency to plantar paw IR irradiation (Kruskal-Wallis test with Mann-Whitney U test; n = 6 mice per group).

‘Thalamic burst’ significantly decreased nociceptive responses of the contralateral paw in von Frey (mechanical) and plantar (thermal) tests (Fig. 38 and 39). Formalin induced nociceptive behaviors were also significantly reduced by ‘Thalamic burst’ (Fig. 40). The first phase behavioral responses (0–5 min) did not differ, but the second phase responses (20–25 min) significantly differed from the other groups (Fig. 40, bar graph). In contrast, iTBS, which was reported to decrease the activity of cortical PV interneurons [61, 62], significantly enhanced nociceptive behaviors in both the first (0–5 min) and second phases (25–30 min), while cTBS has no significant effect (Fig. 38–40). These rTMS results support that nociceptive behaviors could be differentially modulated by TMS protocols designed to mimic endogenous thalamocortical input.

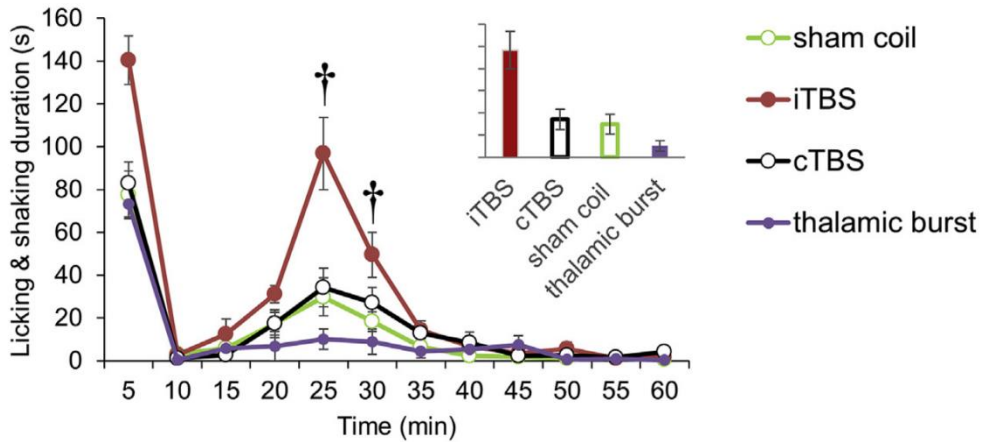


Fig. 40. Formalin-induced inflammatory nociceptive behavior changes to different TMS protocols (repeated measures ANOVA followed by Games Howell post hoc; n = 6 mice per group).

### **3.3 A New Brain Stimulation Method Using Microwave**

New experiences change the connection between the neurons, and these happen not only when people are young but also throughout their lives. It is called neuroplasticity that newly formed neural connections by reorganizing the brain[63]. Neuroplasticity is the reason for rehabilitation as the basic mechanism of learning and memory. Conventional rehabilitation to date has not been directly stimulated the brain, but rather indirectly. Recently, there have been many studies on the improvement of motor function and neuromodulation through direct brain stimulation.

Direct stimulation of the brain can be divided into invasive and non-invasive methods. As a typical invasive method, deep brain stimulation (DBS) inserts a probe into the deep brain region to transmit a signal to a specific neuron [64]. The power to transmit the signal to the probe comes from the implantable pulse generator in the body. The generator's battery should be replaced periodically. Therefore, surgery for brain incision for probe insertion and regular battery replacement is needed.

Noninvasive methods for avoiding surgical operations include repetitive transcranial magnetic stimulation (rTMS) [43]. TMS uses the magnetic field generated by the pulse current flowing in the coil on the head. The alternating magnetic field can induce a current in the brain which stimulates the neuron noninvasively in the brain. TMS device is currently used clinically but has drawbacks such as high cost, high power consumption, and wide magnetic field distribution.

Because the excitatory properties of neurons depend on different cell types, many factors must be considered to understand the effect of given brain stimulation

methods on brain function. However, some characteristics are the same for most neurons. For example, the neurons do not recognize signals over several kHz [54, 58]. Changes in the amplitude of microwave signals were reported to induce changes in brain activity [56, 57]. Repetitive TMS could also change cortical excitability [48]. Our novel brain stimulation method was designed by combining the two concepts. We hypothesized that modulating the microwave signal to form pulse envelopes (see Fig. 41) that has similar frequency to stimulation frequency of rTMS could induce changes in neuronal activity, since neurons have a low-pass filter characteristic [58].

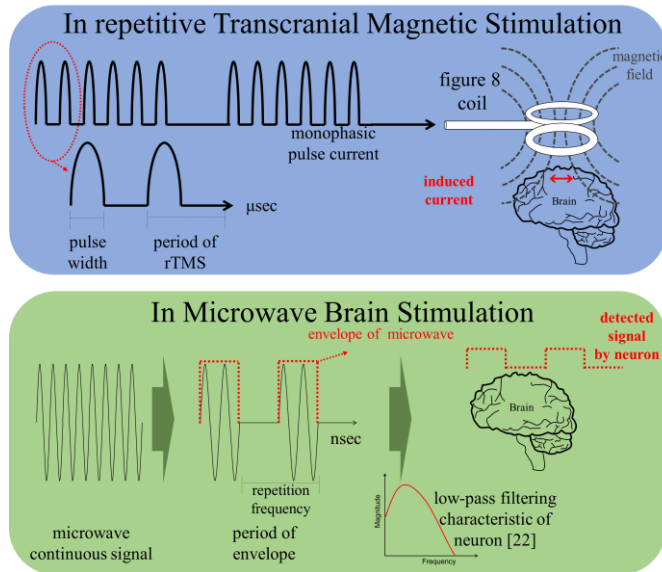


Fig. 41. Concept of brain stimulation via modulated microwave signal.

Fig. 41 depicts the conceptual schematic of stimulating the brain using a pulse envelope modulated microwave signal. Since the envelope of microwave acts as a stimulus signal due to the low pass filter characteristics of neurons, the proposed system would change neuronal activity while spatially restricting the distribution of

an electromagnetic field.

In this chapter, combining the repetition characteristics of rTMS, low-frequency filtering characteristic of neurons, and the short penetration depth of microwaves, we propose a brain stimulation method using microwave signal. The microwave was used as a carrier frequency of a wireless communication system.

### **3.3.1 Pilot Demonstration**

A coaxial line is one of the most commonly used transmission lines in a microwave system [65]. Especially an open-ended coaxial line was used to measure the dielectric constant of living tissue [66]. This is because the electromagnetic wave is not radiated widely from the aperture of the coaxial line but distributed only on the surface, and the permittivity information of the surface can be extracted. There are some issues that need to be addressed in order to use this coaxial line for medical use. The unit cost is important because the applicator used for medical must be used as a disposable part. Therefore, a structure that can be manufactured at low cost while maintaining the characteristics of the coaxial line is required. The stripline operates in the TEM mode at a broadband frequency like a coaxial line and can be fabricated using printed circuit board technology, thus achieving similar performance to a coaxial line at a lower cost. However, since the aperture at the end is determined by the thickness of the substrate, the degree of freedom is reduced. We have brought the cross-section of the coaxial line to a broadside plane to solve this. Fig. 42. depicts a conventional coaxial line, an end-fire type planar applicator, and a broadside-type applicator.

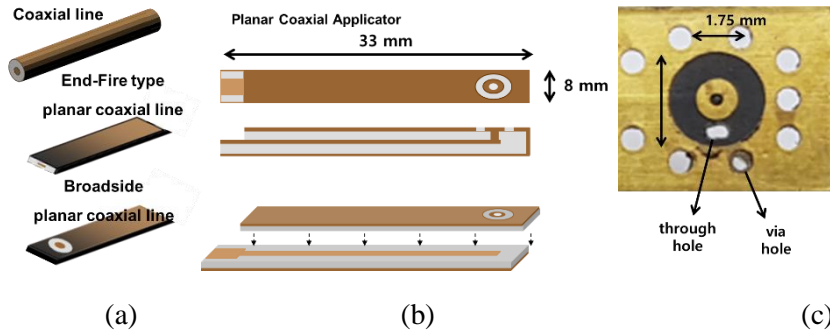


Fig. 42. (a) Conventional and planar type coaxial line, (b) structure of proposed applicator, and (c) photograph of the aperture.

A ring-shaped aperture is made on the broadside of the applicator. The aperture can be manufactured in various sizes and shapes by photolithography. The structure of the applicator is shown in Fig. 42 (b). The signal line of the stripline is connected to the center conductor of the aperture through a metallic via, and the ground is connected to the outer conductor of the aperture. As shown in Fig. 42. (c), the inner and outer diameter are 1.75 mm and 4 mm, respectively.

In brain stimulation, we measured the change of neuronal activity to observe the stimulation effect. A micro-drive consisting of four bundles of four nichrome wire was inserted targeting the hippocampus of the brain. When an electromagnetic field is formed on the aperture of the applicator, the potential of the neuron will change. And the firing rate of the neuron will change. The nichrome wire of the micro-drive will measure the firing rate in the neuron. The hole which the nichrome wire can pass is made. The through hole is 1 mm in diameter. The dimensions of the aperture and through hole were determined by considering the size of the wire and the stimulus range. Fig. 43 shows the result of measuring the  $S_{11}$  when the applicator contacts the brain. The reflection coefficient was the lowest measured at 6.5 GHz.

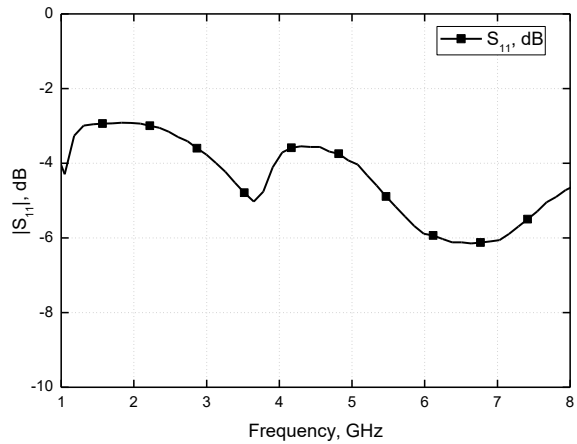


Fig. 43. Measured S-parameter of the applicator.

The brain is an organ that is very sensitive to temperature changes. Therefore, care must be taken not to raise the temperature by the electromagnetic energy during the experiment. However, brain stimulation using microwaves is still an early research stage, and the stimulation mechanisms such as signal amplitude dependence are unknown. Therefore, it is necessary to observe the signal amplitude in real time. Fig. 44 shows the configuration for this experiment.

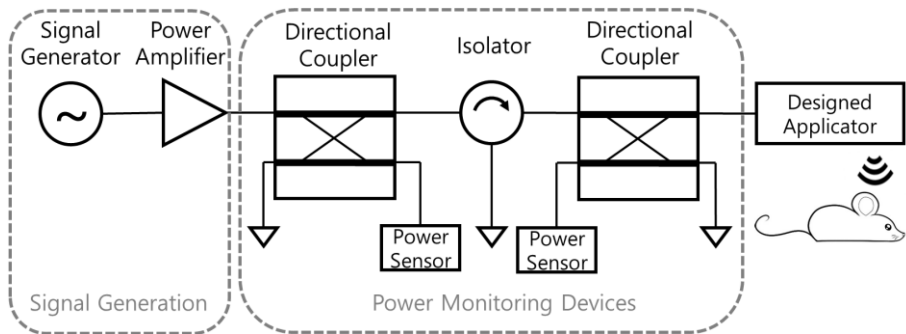


Fig. 44. Experimental setup for brain stimulation using the microwave.

The signal generator (83650B, HP) generated 6.5 GHz to minimize reflection at the proposed applicator. In rTMS, by varying the frequency of repetitive pulses the excitability of the cerebral cortex was different [46]. It has also been reported that there is a correlation between the amplitude modulation of signals in cell phone and brain neuron studies [56, 57]. Therefore, we tried to obtain a similar effect by using the pulse modulation of the microwave signal. In this experiment, two repetition frequencies of 10 Hz and 50 Hz were used. A power amplifier (ZVE-3W-183+, Mini-Circuits) was used to overcome the return loss of the applicator and the insertion loss of the directional coupler and RF cables. The incident and reflected signals were measured using two pairs of directional couplers and a power sensor. A directional coupler next to the power amplifier senses an incident signal of the applicator. And the second coupler measured the reflected signal at the applicator. The isolator prevents the signal reflected from the applicator from returning to the power amplifier.

The applicator delivers a stimulus signal to the brain of the mouse. At the same time, the micro-drive measures the firing rate of the cortical neuron. The nichrome wire of the micro-drive passes through the aperture of applicator. The scalp and skull of the mouse were removed and the cerebrum and aperture of the applicator were directly contacted. In Fig. 45 (a), there is an applicator that is in contact with the cerebrum of the mouse. There is a nichrome wire through the applicator in Fig. 45 (b). Metallic via holes connecting the top and bottom ground of the applicator is larger than the through hole.

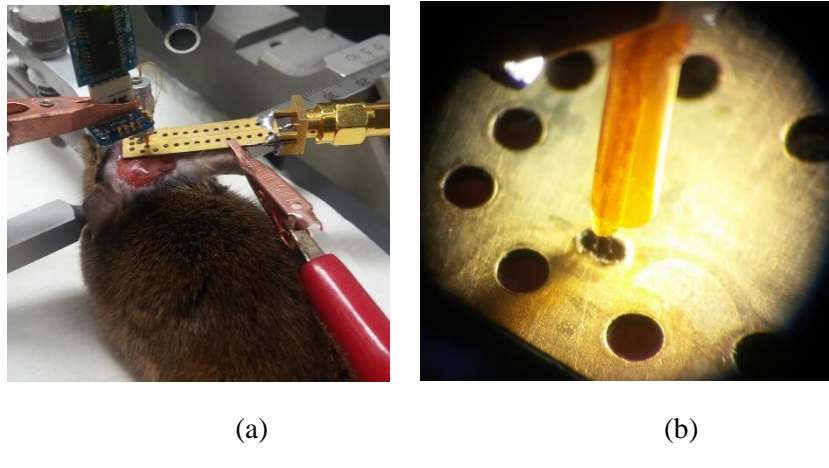


Fig. 45. (a) Experimental setup of mouse, (b) applicator and nichrome wire of micro-drive.

The baseline used the measured firing rate in the unit cell before stimulation. The stimulus signal is a pulse train having a repetition frequency of 10 Hz and 50 Hz having a 50% duty ratio. The power delivered to the brain did not exceed 2 mW. Stimulation lasted for 20 minutes and measuring firing rate was continued after stopping stimulation. Experimental results are presented in Fig. 46.

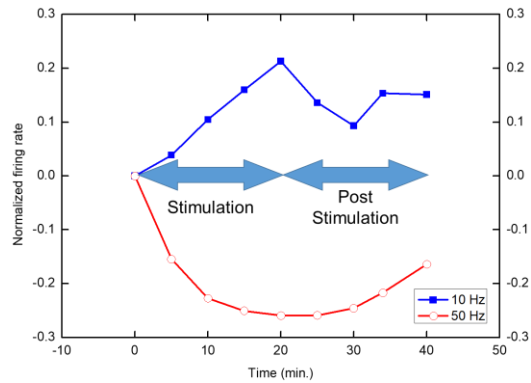


Fig. 46. The stimulation results. The firing rate was measured using micro-drive.

For neuronal activity analysis, the change in the firing rate of individual neurons by stimulation was calculated using the following formula [67].

Normalized firing rate

$$= \frac{\text{firing rate in unit time} - \text{firing rate of baseline}}{\text{firing rate in unit time} + \text{firing rate of baseline}}$$

(11)

Values  $>0$  indicate increased activity, while values  $<0$  indicate decreased activity relative to the baseline. Results showed that the firing tended to decrease in the 50 Hz pulse repetition frequency. In 10 Hz case, the firing rate increased. These changes showed some persistence or slow recovery after the stimulus signal was stopped.

We designed a stimulation applicator for brain stimulation using microwave signal. The applicator is a planar type, and its manufacturing cost is low, making it suitable for medical use. Also, the width and shape of the aperture through which the stimulus signal is transmitted can be freely designed, making it easy to apply for future research. We experimented with brain stimulation using the proposed applicator. A commercial signal generator and a power amplifier were used to generate a stimulus signal with a pulse envelope. Cerebral cortical activity was different according to the repetition frequency of microwave signals transmitted to the cerebrum of a mouse. Microwave brain stimulation, which can regulate the activation/inhibition by adjusting the repetition frequency, offers a new treatment method in the area of neuronal modulation.

### 3.3.2 Microwave Signal Generation Using MMICs

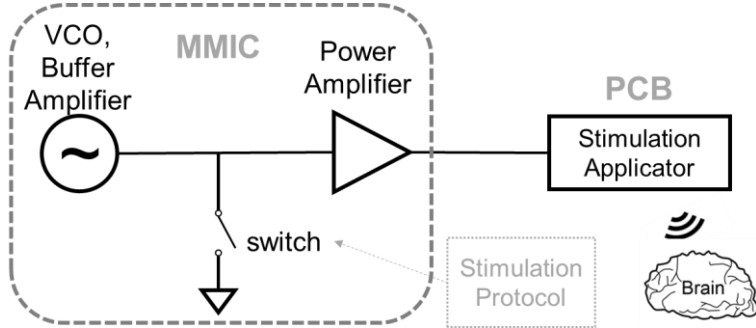


Fig. 47. Overall block diagram of the proposed brain stimulation system

An integrated system has been implemented to demonstrate the feasibility of brain stimulation using modulated microwave signals. Fig. 47 shows an overall block diagram of the proposed brain stimulation system, which consists of a voltage-controlled oscillator (VCO), a switch, a PA, and a stimulation applicator. An oscillator was used to generate microwave signals. The transistor switch, connected to the oscillator, changed the amplitude of the signal to high or low state, so the envelope of the signal becomes a rectangular pulse as in Fig. 41. The pulse envelope signal, amplified by the PA, was delivered to the brain via a stimulation applicator. Details of the circuit are described in the next subsection.

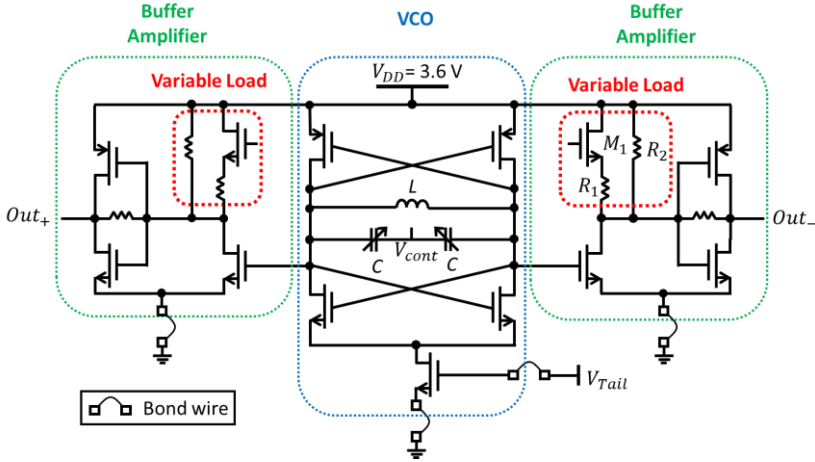


Fig. 48. A schematic of the designed VCO and buffer amplifiers. VCO is made up of n-type MOS and p-type MOS cross-coupled pair and a LC tank.

The VCO, the microwave signal source, generated a microwave signal at 6.5 GHz because this frequency has demonstrated the capability to stimulate the brain activity in the previous study [68]. Schematic drawing of the VCO including buffer amplifiers is shown in Fig. 48. The VCO was designed with a widely adopted n-type metal oxide semiconductor (MOS) and p-type MOS cross-coupled structure [69]. The output frequency was determined by the resonant frequency of the *LC* in the load. The oscillation frequency could be controlled by varying the variable capacitance, *C*, in this schematic. The buffer amplifier was used to prevent the *LC* resonance frequency changing due to changes in the impedance seen at the VCO output.

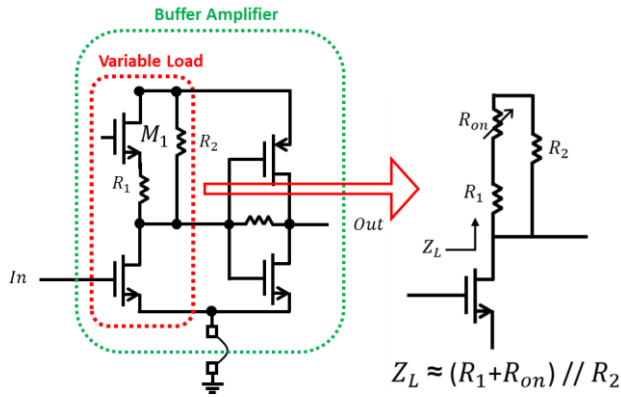


Fig. 49. A buffer amplifier has variable load. Equivalent load impedance has a value between  $R_2$  and  $R_1//R_2$  depending on the state of the transistor  $M_1$ .

The buffer amplifier had a variable load, allowing control of the output power. The power control was able to observe the stimulation effect, according to the amplitude change of the stimulus signal. Fig. +49 shows the buffer amplifier and equivalent circuit of a variable load. Loads of the common source included resistors  $R_1$  and  $R_2$  and transistor  $M_1$ . The transistor  $M_1$  operated as a variable resistor. When the gate voltage was close to  $V_{DD}$ , the  $M_1$  turned on and the on-resistance of  $M_1$  became very small so that the equivalent resistance became  $R_1//R_2$ . When the gate voltage reached zero, the  $M_1$  became off and the  $R_2$  value was seen. As a result, gate voltage of  $M_1$  determined the load impedance between  $R_2$  and  $R_1//R_2$ . The output power was controlled by changing load impedance of the common source amplifier.

### 3.3.3 Waveform Modulation and Power Amplification

The microwave signal from the buffer amplifier was sent to the PA once its waveform was modulated by the transistor switches. As described in section II, the switch of Fig. 47 turned the envelope of the microwave signal into a rectangular pulse shape according to the on/off state. The switch was connected in parallel to prevent signal loss due to on-resistance of transistor. Applying a brain stimulation protocol, such as rTMS [48], to the gate of the switching transistor produced a modulated microwave signals.

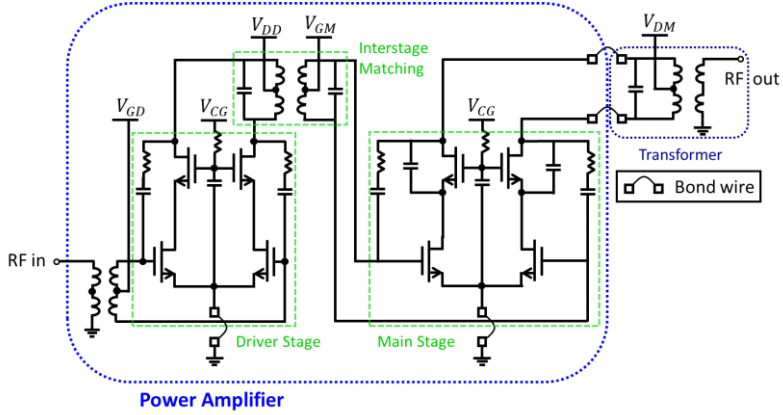


Fig. 50. Schematic diagram of the designed PA and transformer.

Since brain cells are vulnerable to elevations of temperature [70-72], the maximum power of microwave signal was adjusted to 20 dBm using the PA. According to our simulation results, the designed VCO generated the output power around 0 dBm. It was required to amplify the microwave signal by 20 dB. Considering the maximum available gain of the 0.28- $\mu$ m silicon on insulator (SOI) complementary MOS (CMOS) field effect transistor at 6.5 GHz, 2-stage design

approach was adopted for the PA. To avoid the source degeneration, which generally degrades the performance of the PA, differential structure was used. A schematic of the PA is shown in Fig. 50.

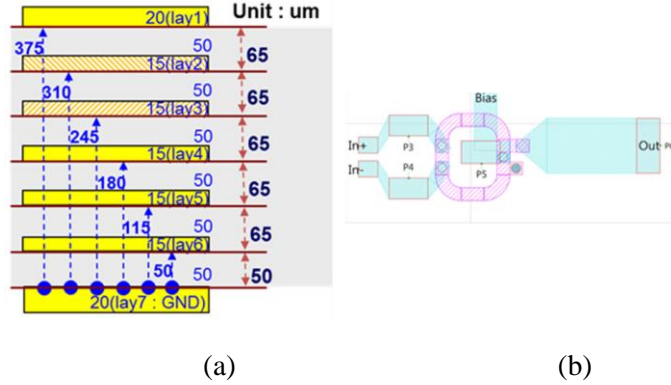


Fig. 51. (a) Cross-sectional view of the seven-layer PCB, (b) layout of the transformer.

A transformer converted the differential signal of the PA into a single-ended signal. When a transformer was manufactured in the CMOS process, there was a huge conduction loss because the metal was quite thin; this lowered the output power of the brain stimulation system and reduced power efficiency. Therefore, a seven-layer printed circuit board (PCB) was used to solve this problem. The layer information of the PCB is shown in Fig. 51 (a). Layers used as transformers were *lay2* and *lay3*. This was 3.75 times greater than the maximum thickness provided in a SOI CMOS process. The top layer metal had the lowest conduction loss because it was the thickest, but it was not used to minimize interference with external circuit components. Fig. 51 (b) shows the layout of the transformer.

### 3.3.4 Integrated Brain Stimulation System

Bonding wires were typically used to connect the integrated circuit (IC) to the PCB or other ICs. When the VCO and switch chip were separately fabricated and connected by a bonding wire, the isolation characteristic of the switch is degraded due to the inductance of the bonding wire. To solve this isolation problem and ultimately facilitate integration, the VCO, buffer amplifier, switches, and PA were integrated onto one chip. Fig. 52 (a) shows a photograph of the fabricated stimulation system module. An integrated chip was fabricated using a 0.28- $\mu\text{m}$  SOI CMOS process. The size of the entire chip and module were 1.38 mm  $\times$  0.91 mm and 30 mm  $\times$  30 mm, respectively. Fig. 52 (b) shows an enlarged photograph of entire CMOS chip and the transformer.

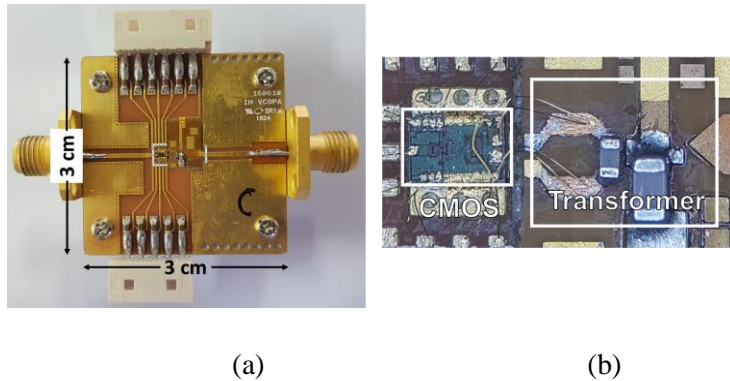


Fig. 52. Photograph of stimulation system. (a) Integrated IC and biasing PCB. (b) Enlarged photograph of the CMOS and transformer.

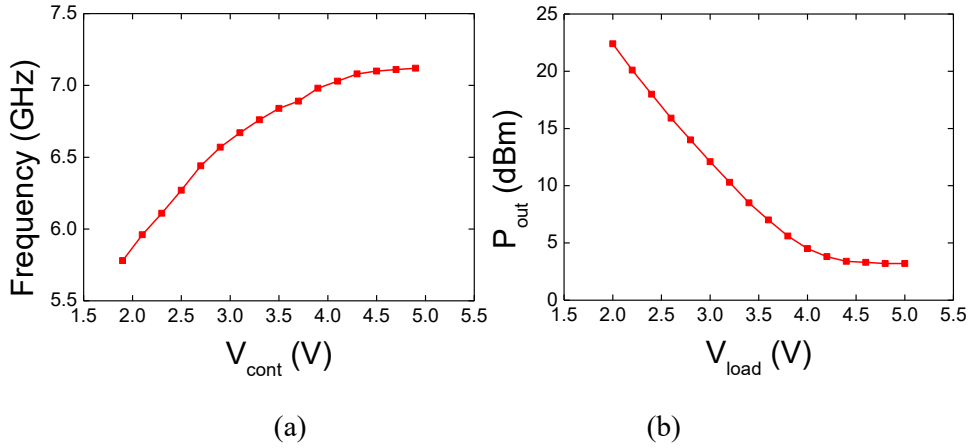


Fig. 53. Measured results of the stimulation system. (a) Frequency tuning range, (b) output power.

Fig. 53 (a) and 53(b) show the measured output signal of the stimulation system. As a result, the frequency tuning range was 5.7–7.12 GHz. When the modulation switch was turned off, the output power varied, from 3.2–22.4 dBm, at 6.5 GHz.

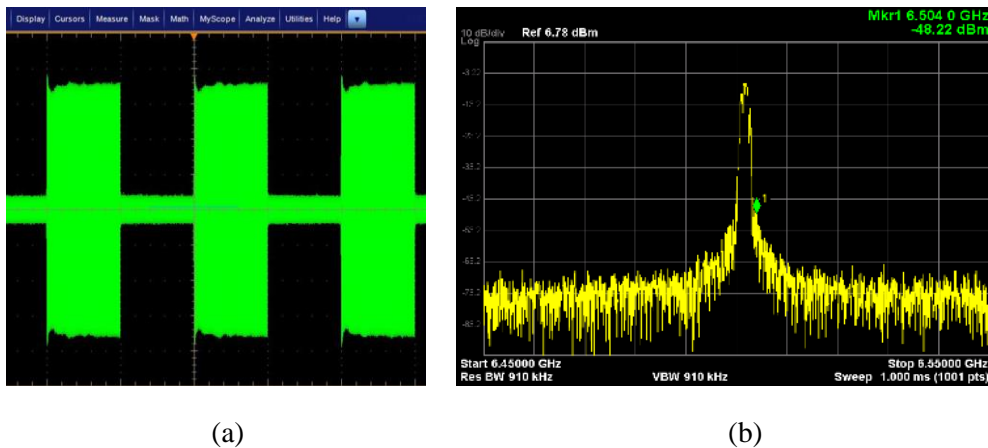


Fig. 54. The modulated microwave signal in time domain and frequency domain  
(a) measured result in time domain, (b) measured result in frequency domain.

We confirmed that the continuous signal was modulated when rectangular pulses were applied to the system. Rectangular pulses, which has a 1 MHz pulse with 50% duty cycle, was used as the stimulation protocol. Fig. 54 (a) shows the actual measurement, measured using an oscilloscope (DPO71604C, Tektronix). When the protocol was applied, an average power of the signal was reduced by 3 dB (50%) compared to the continuous signal and the pulse envelope signal has approximately 17 dB isolation. Fig. 54 (b) shows the frequency component of 6.5 GHz as a result of the measurement with a spectrum analyzer (N9020A, Agilent). Clinical stimulation protocols of rTMS or theta burst stimulation (TBS) usually use low frequency of < 100 Hz. However, the proposed brain stimulation system could generate stimulus signals over a wide frequency range up to 1 MHz, including the stimulation protocols used for rTMS or TBS.

### 3.3.5 Stimulation Applicator

The proposed system required a stimulation applicator that could deliver microwave signals to the brain with low return loss. Physical size and weight of the applicator were also considered. To stimulate the brain of small animals, such as a mouse, the applicator should be small enough to be placed on top of the head and should be light-weight so that animals could move freely.

A PCB was used as a material to fulfill the weight requirement, and *LC* resonance structure was adopted as the topology of the applicator to facilitate resonance frequency control. For example, the resonance frequency was easily adjustable by adjusting a length of the stub inductor and width of gap capacitor.

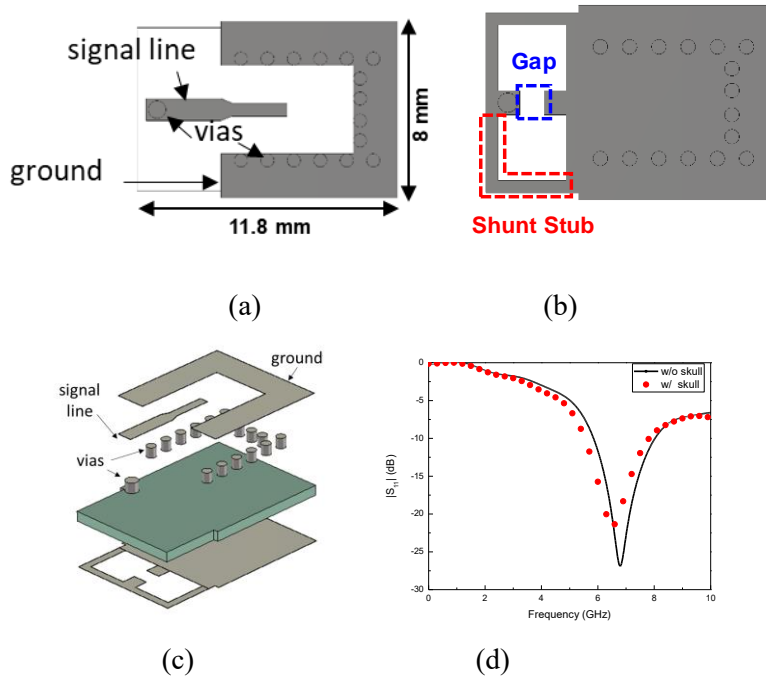


Fig. 55. Stimulation applicator. (a) Upper plane, (b) lower plane, (c) oblique view, and (d) s-parameter of the simulation result.

The detailed structure of an applicator, using a *LC* tank that consisted of a gap capacitor and shunt stub inductor, is shown in Fig. 55. The overall size of the applicator is 11.8 mm × 8 mm. Fig. 55 (a) depicts the upper plane of the substrate which is composed of a ground and a signal line. The “ $\supset$ ” shaped ground was connected to the bottom ground by metallic via holes. The signal line was a straight line whose width varies to satisfy the characteristic impedance of 50 ohms. At the left end of the signal line, a hollow metallic via hole was connected to the conductor of the lower plane. Fig. 55 (b) shows the bottom of the PCB. The signal, transmitted to the bottom of the substrate through the via hole in the signal line, met the gap capacitor and the shunt stub inductor to induce a resonance. The width and spacing of the gap capacitor was easily adjustable in accordance with the area intended for stimulation. In this paper, the size of the gap was defined as 1 mm × 1 mm, since it was suitable for targeting a specific brain area, the hippocampus. The length of the stub was adjusted to match the resonance frequency. The whole conductor, located at the lower plane of the substrate was insulated to prevent electrical currents from accidentally flowing into the brain. RT/Duroid 3010 (Rogers corp.), with a high dielectric constant ( $\epsilon_r=10.2$ ), was selected to increase capacitance in the gap and minimize the length of the shunt stub. Fig. 55 (c) shows a full perspective view of the applicator. Its thickness was 0.635 mm for tight attachment to the surface of the brain. In addition, it only weighted 0.25 g, which was light enough to be mounted on a mouse brain. The applicator was designed using a commercial three-dimensional electromagnetic simulation program (CST microwave studio 2017). For simplicity, the brain models were assumed to be spherical and homogeneous dielectric constants. The simulation results showed that the skull did not affect the pattern of

electromagnetic field distribution. The return loss was optimized to the smallest value when the gap of the applicator contacted on the brain after part of a skull was removed. Fig. 55 (d) shows the reflection coefficient of the applicator, optimized for the mouse brain model, which had the lowest reflection at 6.5 GHz.

### 3.3.6 Mouse Experiments

Mice were used to determine the feasibility of the brain stimulation using pulse envelope microwave signal. The experimental setup, using the proposed stimulation system and applicator, is shown in Fig. 56. We connected a commercial power monitoring devices between the system and an applicator to measure the signal power. Two pairs of coupler (158020, Krytar) and a power meter (E4417A, Agilent) were used to separate the incident and reflected powers, and an isolator (DMI6018, DiTom Microwave) was used to isolate them. Detailed settings for measuring incident and reflected powers can be found in [73]. By measuring incident and reflected powers, the power delivered from the applicator to the brain was calculated. In this experiment, the delivered power was approximately 8.73 dBm (7.46 mW).

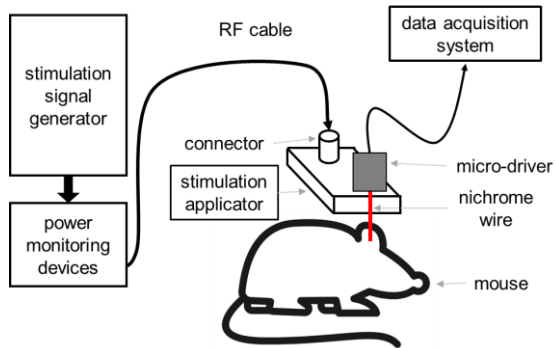


Fig. 56. Experimental setup consisting of the proposed stimulation signal generator and an applicator.

Mice anesthetized with urethane were used to measure the effect of stimulation on the activity of individual hippocampal neurons in the brain. Total four mice were used as stimulation group to which the stimulation signals were delivered. Other four mice were used as control group that underwent the same procedure except for the

stimulation delivery. The head of each mouse was fixed with a small animal stereotaxic instrument (Kopf, USA) for precise stimulation and recording of the target brain region. After removing the skull above the target region, a stimulation applicator was placed to be in direct contact with the brain. Then, nichrome wires of a micro-drive were inserted into the target brain area through a via hole in the signal line of the applicator to record electrophysiological activity of neurons in the brain [74].

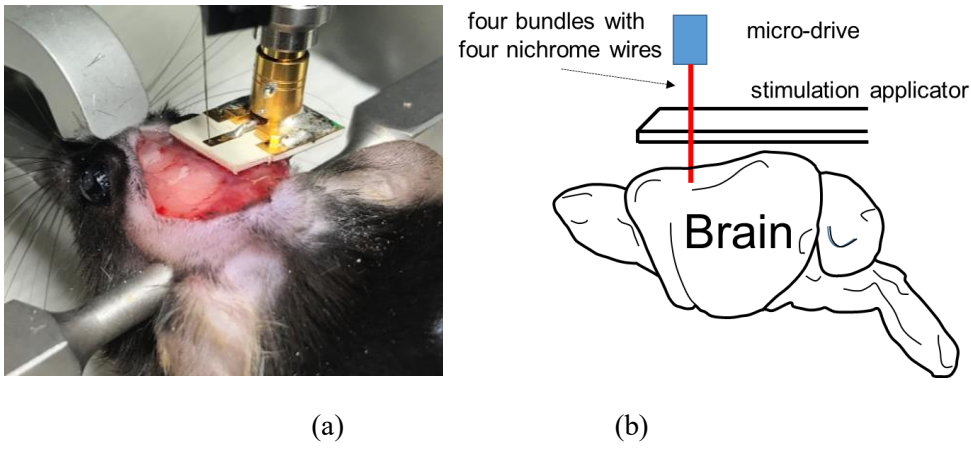


Fig. 57. (a) Photograph of the stimulation applicator and nichrome wires of a micro-drive. (b) illustration to help understand the placement of the applicator and micro-drive.

Fig. 57 (a) shows a photograph of an applicator placed on top of a mouse brain with nichrome wires ( $12 \mu\text{m}$  in diameter) to measure neuronal activity changes induced by the microwave stimulation. Wires were mounted in a micro-drive to adjust the recording depth in the brain. Fig. 57 (b) figuratively depicts nichrome wires for recording neuronal activity, placed through a hollow metallic via hole in

the signal line of the applicator. Brain stimulation and neuronal activity recording was carried out simultaneously to investigate the direct effect of the new brain stimulation method.

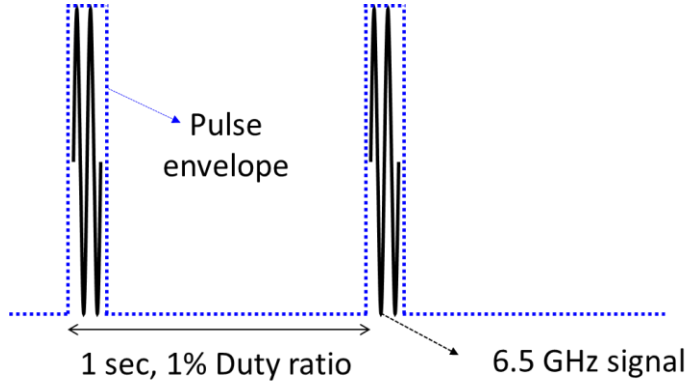


Fig. 58. Waveform of the modulated microwave signal used in this work.

Microwave signals were delivered in pulse envelopes (10 msec width, 1 Hz repetition). Fig. 58 shows a simplified waveform of the signal used for brain stimulation. The modulation switch operated for 10 msec and repeated every 1 sec. As a result, the envelope of the microwave signal had a rectangular pulse shape of 1% duty cycle.

Single unit data was sorted and confirmed to be isolated from the noise. Then, recorded data of CA1 pyramidal neurons in the hippocampus was used for the further analysis. In total, 34 neurons from stimulation group and 18 neurons from control group were recorded respectively. To assess the effect of stimulation on neuronal activity, firing rates of neurons were recorded for 40 minutes: before (10 min: baseline), during (20 min: during stimulation session, 10msec-width pulse) and after (10 min: after stimulation session) a stimulation. In control group, the first 10 min

data were used as baseline from total 40 min recording to measure the time effect during the experimental procedure on firing activity for comparison.

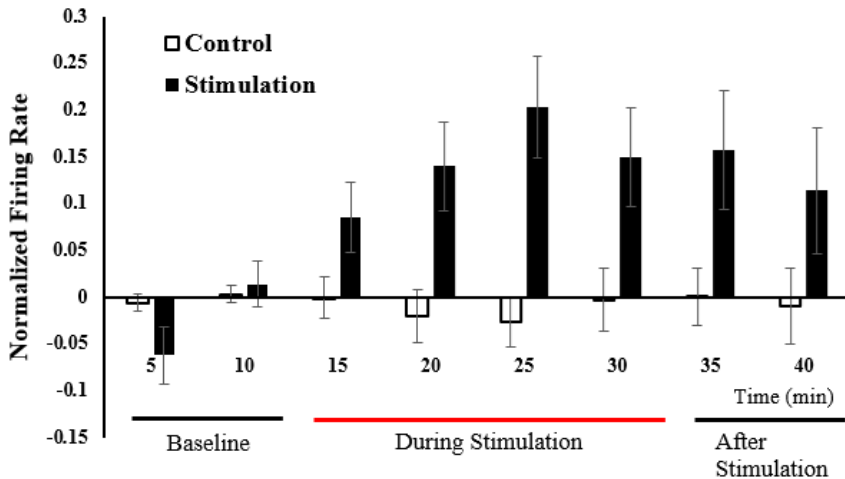


Fig. 59. Cellular response to the modulated microwave signal. Positive value indicates excitation, while negative value indicates inhibition of neuronal activity. Normalization was based on the baseline firing rate. (N= 34 neurons, 4 mice in stimulation group; N=18 neurons, 4 mice in control group)

The effect of the modulated microwave signal on brain stimulation was observed by comparing firing rates before (baseline), during, and after stimulation. Fig. 59 shows the results of normalized firing rates relative to the baseline. [67]. During stimulation session, the stimulation group that received repetitive 1 Hz stimulation showed significantly excited neuronal activity as the stimulation time elapsed whereas the control group did not show any differences. (Two-way ANOVA with repeated measures; significant effect of group,  $F_{(1,50)}=5.718$ ,  $P=0.021$ ; significant effect of group\*time interaction,  $F_{(2,072,103.591)}=4.384$ ,  $P=0.014$ ; no significant effect

of stimulation time,  $F_{(2,07,103,591)}=1.978$ ,  $P=0.142$ ) (Fig. 14). Enhanced neuronal activity induced by stimulation persisted for a short time after the stimulation was turned off (after-stimulation session).

TABLE III. Neuronal activities of each sessions

Session	Raw firing rate (Hz)		Normalized firing rate	
	Control	Stimulation	Control	Stimulation
Baseline	0.46±0.069	0.40±0.070		
During stimulation I First phase (0-10 min)	0.44±0.074	0.46±0.087	-0.01±0.024	0.12±0.042
During stimulation II Second phase (10-20 min)	0.45±0.078	0.53±0.087	0.01±0.029	0.18±0.053
After stimulation	0.48±0.083	0.52±0.109	-0.002±0.0335	0.15±0.064

Table III summarizes the averaged raw data of firing rate (Hz) ± S.E.M and the averaged normalized values ± S.E.M relatively to the baseline during each session. This result implies that the duration of stimulation significantly correlates with the magnitude of neuronal activity increase (Fig 59.). Moreover, the after-stimulation session shows that enhanced neuronal activity remained for a short time even after stimulation has ended. This result indicates that the stimulation has immediate and lasting effects that influence the activity of neurons.

After confirming effects of the stimulation in neuronal activity, we investigated whether temperature may have, or may not have, influenced the results, since brain

activity is sensitive to temperature changes. Increase of brain temperature by 6°C to 8°C caused irreversible damage to brain tissues and a rise by 1.5-3°C noticeably affected neuronal activities [70-72]. Microwave energy could generate frictional heat by rotating water molecules in the brain; this heat, if any, could have caused changes in the activity of neurons. Therefore, we measured temperature changes in the brain before, during, and after stimulation. A fiber optical thermometer (m822, Luxtron), unlike the conductor thermometer, that does not change the boundary conditions of the electromagnetic field was used. The result of brain temperature measurement, when the delivered power is equal to the stimulus signal, showed that no temperature changes were induced by the stimulation used in this study (Fig. 60). This confirms that the temperature changes did not cause the activity of neurons to change, and strongly suggest that electromagnetic field amplitude of the new stimulation method may have been the sole factor causing the firing rate of neurons to increase.

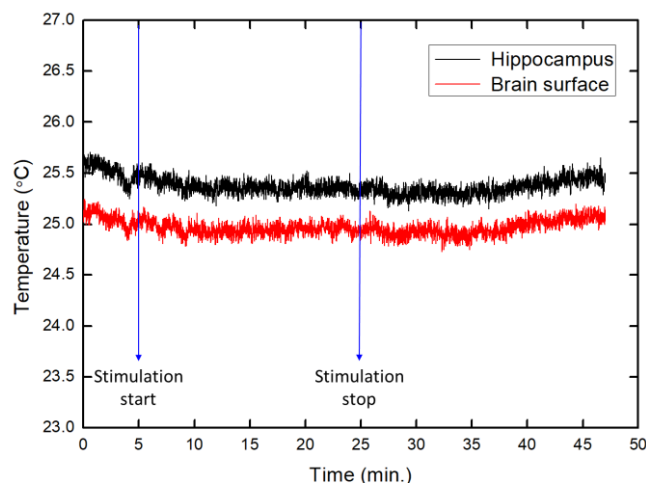


Fig. 60. Changes in temperature in the hippocampus and on the brain surface when microwave energy is delivered to the brain.

## Chapter 4 Conclusion

In this dissertation, human body application using RF/microwave have been studied. The first is the hyperthermia using magnetic nanoparticles, and the second is about the neuronal stimulation.

Magnetic nanoclusters with various size distributions were synthesized, and their physical properties were confirmed by TEM, DLS, and XRD. Especially, in order to confirm the characteristics of frequency dependence, the AC magnetization curve was measured, and the relaxation loss was found to increase with increasing frequency. A lab-made magnetic field generator was used to measure the SLP according to the magnetic field strength and frequencies. In the temperature measurement of the MNC solution, it was found that the magnetic field strength required to overcome the energy barrier which depends on the size of the magnetic particles. The 60 nm MNC exhibited a significant increase in temperature within 10 min for inducing cell death compared to different size MNCs. It was experimentally confirmed that the viability of the cells when MNC-absorbed CSCs were exposed to an AMF was remarkably reduced in a short time. Seven nude mice were used for the *in vivo* test. In the control and sham-treatment groups, the volume of cancer cells continued to increase, but the MFH treatment group gradually decreased and destroyed was confirmed. Although there are some remaining cancers, MFH have shown good therapeutic results. The method presented in this study can be used as an auxiliary means of cancer treatment.

Secondly we propose a new non-invasive method to stimulate neurons in the brain. We added a modulation switch to a signal generator to create pulse envelopes. Then,

we fabricated a signal generator (VCO), modulator (switches), and PA as a CMOS process and integrated it into a single chip. The stimulation applicator was a small, lightweight, and simple *LC* structure that generates an electric field in a narrow area of brain. Therefore, the proposed applicator is suitable for attachment onto the head of a mouse to transmit brain stimulation signals, and possibly onto the skull in the future. The effect of modulated microwave signal on brain activity was evaluated by measuring the activity of individual neurons in mice. Before, during, and after stimulation, neuronal activity changes were measured and analyzed. Stimulation gradually and significantly increased neuronal activity over time. The effects persisted for a while after the 20-min stimulation had stopped.

Our results demonstrate that modulated microwave with pulse envelopes is an effective method to stimulate neurons. It offers several advantages over conventional brain stimulation methods. The proposed system limits the distribution of the electromagnetic field to a narrow region. The power consumption is also very low compared to other studies on TMS effects using small animals [75]. Because this study was carried out in mice the system consumed very low power, approximately 7.46 mW, but human brain stimulation may require greater power, estimated to be less than 1 W. Nonetheless, power consumption of the new stimulation method is extremely low compared to the conventional TMS devices which consumes about 400 W (eXimia TMS,      Nexstim). The stimulation applicator is also easy to adjust, in terms of the various range of stimulation area. In addition, as the pulse width and the frequency of repetition of the envelope can be easily adjustable, testing several different stimulation protocols, which may have different effect, is readily available.

Further studies, such as testing the effect of changes in carrier frequency or

amplitude of signal to develop new protocols for different purposes, should be carried out to verify and establish application of the new brain stimulation method. The new stimulation method using modulated microwave offers a promising new brain stimulation method with low-power consumption, focused stimulation area, and easily adjustable stimulation patterns.

# Appendix

## High Resolution TEM Images

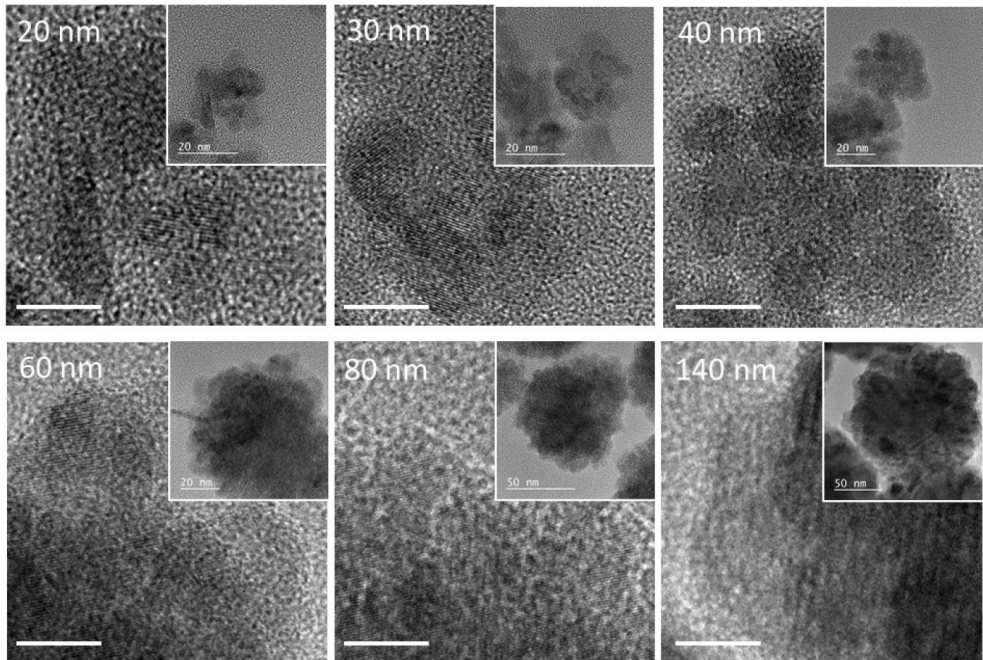


Fig. A1. HR-TEM images.

HR-TEM images of the various sized MNC particles. From the image, all MNC particles were revealed high crystallinity and formed with aggregation of primary crystalline. The scale bar is indicated to the 5 nm and inset image is for the relatively low magnification of HR-TEM image.

## Fields of Finite Solenoid Coil – calculation off the axis

The magnetic field due to solenoid coil is given in terms of the magnetic vector potential  $\bar{A}$  by:

$$\bar{B} = \nabla \times \bar{A} \quad (\text{A. 1})$$

$\because \bar{B}$  has solenoid nature ( $\nabla \cdot \bar{B} = 0$ ) and from vector identity  $\nabla \cdot \nabla \times \bar{A} = 0$ ,  
 $\bar{B} = \nabla \times \bar{A}$  can be derived.

In Cylindrical coordinates ( $r, \phi, z$ )

$$\begin{aligned} \nabla \times \bar{A} &= \frac{1}{r} \begin{vmatrix} \bar{a}_r & \bar{a}_\phi & \bar{a}_z \\ \frac{\partial}{\partial r} & \frac{\partial}{\partial \phi} & \frac{\partial}{\partial z} \\ A_r & rA_\phi & A_z \end{vmatrix} \\ &= \bar{a}_r \left( \frac{\partial A_z}{r \partial \phi} - \frac{\partial A_\phi}{\partial z} \right) + \bar{a}_\phi \left( \frac{\partial A_r}{\partial z} - \frac{\partial A_z}{\partial r} \right) + \bar{a}_z \frac{1}{r} \left( \frac{\partial (rA_\phi)}{\partial r} - \frac{\partial A_r}{\partial \phi} \right) \end{aligned} \quad (\text{A. 2})$$

For the geometry assumed, only the  $A_\phi$  component can be nonzero. Then (A. 1) yields simply

$$B_r = -\frac{\partial A_\phi}{\partial z}, \quad B_z = \frac{1}{r} \frac{\partial (rA_\phi)}{\partial r} = \frac{1}{r} A_\phi + \frac{\partial A_\phi}{\partial r} \quad (\text{A. 3})$$

From [27] [5.5 Vector Potential and Magnetic Induction for a Circular Current Loop. pp. 181] Circular loop of radius  $a$ , lying in the  $x$ - $y$  plane, centered at the origin, and carrying a current  $I$ , as shown below.

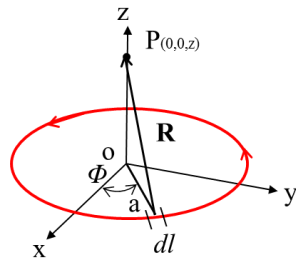


Fig. A2. A circular loop carrying current  $I$ .

The current density  $\bar{J}$  has only a component in the  $\phi$  direction.

$$\bar{J} = I \sin \theta' \delta(\cos \theta') \frac{\delta(r' - a)}{a} \quad (\text{A. 4})$$

The delta functions restrict current flow to a ring of radius  $a$ .

$$\bar{J} = \begin{bmatrix} \cos \phi' & -\sin \phi' & 0 \\ \sin \phi' & \cos \phi' & 0 \\ 0 & 0 & 1 \end{bmatrix} \begin{bmatrix} 0 \\ J_\phi \\ 0 \end{bmatrix} = \bar{a}_x (-\sin \phi') J_\phi + \bar{a}_y (\cos \phi') J_\phi \quad (\text{A. 5})$$

Processs of finding  $A_\phi$

$$A_\phi = \frac{\mu_0}{2\pi} \frac{Ia}{L} \left[ \int_0^\pi \cos \phi' \cdot \ln(\zeta + \alpha(\zeta)) d\phi' \right]_{\zeta_-}^{\zeta_+} \quad (\text{A. 6})$$

$$\text{where, } \alpha(\zeta) = \sqrt{\zeta^2 + a^2 + \rho^2 - 2a\rho \cos \phi'}.$$

Integration by parts

$$\begin{aligned} & \int_0^\pi \cos \phi' \cdot \ln(\zeta + \alpha(\zeta)) d\phi' \\ &= \sin \phi' \cdot \ln(\zeta + \alpha(\zeta)) \Big|_0^\pi - \int_0^\pi \sin \phi' \cdot \frac{d}{d\phi'} \ln(\zeta + \alpha(\zeta)) d\phi' \end{aligned} \quad (\text{A. 7})$$

The first term is zero, and the derivative of  $\ln(\zeta + \alpha(\zeta))$  is:

$$\begin{aligned} & \frac{\partial}{\partial \phi'} \ln(\zeta + \alpha(\zeta)) \\ &= \frac{1}{\zeta + \alpha(\zeta)} \cdot \frac{1}{2} (\zeta^2 + \rho^2 + a^2 - 2a\rho \cos \phi')^{-\frac{1}{2}} \cdot (2a\rho \sin \phi') \\ &= \frac{1}{\zeta + \alpha(\zeta)} \cdot \frac{1}{2} \frac{1}{\alpha(\zeta)} \cdot (2a\rho \sin \phi') \\ &= \frac{a\rho \sin \phi'}{(\zeta + \alpha(\zeta)) \cdot \alpha(\zeta)} \end{aligned} \quad (\text{A. 8})$$

Multiple by  $\frac{(\alpha(\zeta)-\zeta)}{(\alpha(\zeta)+\zeta)}$ .

$$\begin{aligned}
 & \frac{a\rho \sin \phi'}{(\zeta + \alpha(\zeta)) \cdot \alpha(\zeta)} \cdot \frac{(\alpha(\zeta)-\zeta)}{(\alpha(\zeta)+\zeta)} \\
 &= \frac{a\rho \sin \phi' (\alpha(\zeta)-\zeta)}{(\alpha^2(\zeta)-\zeta^2) \alpha(\zeta)} \\
 &= \frac{a\rho \sin \phi' (\alpha(\zeta)-\zeta)}{\alpha(\zeta)(\rho^2 + a^2 - 2a\rho \cos \phi')} \\
 &= \frac{a\rho \sin \phi'}{(\rho^2 + a^2 - 2a\rho \cos \phi')} + \frac{-a\rho \zeta \sin \phi'}{\alpha(\zeta)(\rho^2 + a^2 - 2a\rho \cos \phi')} \tag{A. 9}
 \end{aligned}$$

The first term on the right side appeared on both  $\alpha_{\pm}$ , then

$$\begin{aligned}
 & \int_0^\pi \sin \phi' \cdot \frac{d \ln(\zeta + \alpha(\zeta))}{d\phi'} d\phi' \\
 &= - \int_0^\pi \sin \phi' \cdot \frac{-a\rho \zeta \sin^2 \phi'}{\alpha(\zeta)(\rho^2 + a^2 - 2a\rho \cos \phi')} d\phi' \tag{A. 10}
 \end{aligned}$$

Finally, the (A. 6) is summarized as follows

$$\begin{aligned}
 A_\phi &= \frac{\mu_0}{2\pi} \frac{Ia}{L} \left[ \int_0^\pi \cos \phi' \cdot \ln(\zeta + \alpha(\zeta)) d\phi' \right]_{\zeta_-}^{\zeta_+} \\
 &= \frac{\mu_0}{2\pi} \frac{Ia}{L} \left[ \int_0^\pi \frac{a\rho \zeta \sin^2 \phi'}{\alpha(\zeta)(\rho^2 + a^2 - 2a\rho \cos \phi')} d\phi' \right]_{\zeta_-}^{\zeta_+} \tag{A. 11}
 \end{aligned}$$

$B_r$  can be obtained from (A. 3)

$$B_r = -\frac{\partial}{\partial z} A_\phi = -\frac{\partial}{\partial \zeta} A_\phi \quad (\text{A. 12})$$

$$\ddot{\equiv} \frac{d}{dx} \int_a^b f(x) dx = f(b) - f(a)$$

First, the natural logarithm of the (A. 6) is differentiated as follows.

$$\begin{aligned} \frac{\partial}{\partial \zeta} \ln(\zeta + \alpha(\zeta)) &= \frac{1}{\zeta + \alpha(\zeta)} \cdot (1 + \alpha'(\zeta)) \\ &= \frac{1}{\zeta + \alpha(\zeta)} \cdot \left( 1 + \frac{1}{2} (\zeta^2 + a^2 + \rho^2 - 2a\rho \cos(\phi'))^{\frac{1}{2}} \cdot 2\zeta \right) \\ &= \frac{1}{\zeta + \alpha(\zeta)} \left( 1 + \frac{\zeta}{\alpha(\zeta)} \right) = \frac{1}{\zeta + \alpha(\zeta)} \frac{\zeta + \alpha(\zeta)}{\alpha(\zeta)} \\ &= \frac{1}{\alpha(\zeta)} \end{aligned} \quad (\text{A. 13})$$

Substituting this into (A. 12),

$$\begin{aligned} B_r &= -\frac{\partial}{\partial \zeta} \frac{\mu_0}{2\pi} \frac{Ia}{L} \left[ \int_0^\pi \cos \phi' \cdot \ln(\zeta + \alpha(\zeta)) d\phi' \right]_{\zeta_-}^{\zeta_+} \\ &= -\frac{\mu_0}{2\pi} \frac{Ia}{L} \left[ \int_0^\pi \cos \phi' \cdot \frac{1}{\alpha(\zeta)} d\phi' \right]_{\zeta_-}^{\zeta_+} \\ &= -\frac{\mu_0}{2\pi} \frac{Ia}{L} \left[ \int_0^\pi \cos \phi' \cdot \frac{1}{\sqrt{a^2 + \rho^2 + \zeta^2 - 2a\rho \cos \phi'}} d\phi' \right]_{\zeta_-}^{\zeta_+} \end{aligned} \quad (\text{A. 14})$$

(A. 14) describe the magnetic field due to a finite solenoid. Numerical results can be readily be found by integrating these equations on a computer. However, the result can also be expressed in terms of standard elliptic integrals. The following relationship is used to derive the elliptic integral form.

$$F(\pi) - F(0) = \int_0^\pi f(\cos\phi') d\phi' = \int_0^{-\pi} f(\cos\phi') d\phi' = \int_0^\pi f(-\cos t) (-dt) \quad (\text{A. 15})$$

$$\begin{aligned} B_r &= -\frac{\mu_0}{2\pi} \frac{Ia}{L} \left[ \int_0^\pi \cos\phi' \cdot \frac{1}{\sqrt{a^2 + \rho^2 + \zeta^2 - 2a\rho\cos\phi'}} d\phi' \right]_{\zeta_-}^{\zeta_+} \\ &= -\frac{\mu_0}{2\pi} \frac{Ia}{L} \left[ \int_0^\pi \frac{-\cos\phi'}{\sqrt{a^2 + \rho^2 + \zeta^2 + 2a\rho\cos\phi'}} (-d\phi') \right]_{\zeta_-}^{\zeta_+} \\ &= -\frac{\mu_0}{2\pi} \frac{Ia}{L} \left[ \int_0^\pi \frac{\cos\phi'}{\sqrt{(a+\rho)^2 + \zeta^2 - 2a\rho + 2a\rho\cos\phi'}} d\phi' \right]_{\zeta_-}^{\zeta_+} \end{aligned} \quad (\text{A. 16})$$

By using the change of integration interval ( $\phi' = 2\theta$ )

※ Trigonometric formula

$$\cos 2\theta = 1 - 2\sin^2 \theta = \cos^2 \theta - \sin^2 \theta = 2\cos^2 \theta - 1$$

$$\begin{aligned} B_r &= -\frac{\mu_0}{2\pi} \frac{Ia}{L} \left[ \int_0^\pi \frac{\cos\phi'}{\sqrt{(a+\rho)^2 + \zeta^2 - 2a\rho + 2a\rho\cos\phi'}} d\phi' \right]_{\zeta_-}^{\zeta_+} \\ &= -\frac{\mu_0}{2\pi} \frac{Ia}{L} \int_0^{\frac{\pi}{2}} \frac{1 - 2\sin^2 \theta}{\sqrt{(a+\rho)^2 + \zeta^2 - 4a\rho\sin^2 \theta}} (2d\theta) \end{aligned} \quad (\text{A. 17})$$

Here, substitute the following into (A. 17)

$$k^2 = \frac{4a\rho}{(a+\rho)^2 + \zeta^2}$$

Finally, the  $B_r$  is summarized as follows.

$$\begin{aligned}
B_r &= -\frac{\mu_0}{2\pi} \frac{Ia}{L} \int_0^{\frac{\pi}{2}} \frac{1-2\sin^2\theta}{\sqrt{(a+\rho)^2 + \zeta^2 - 4a\rho\sin^2\theta}} (2d\theta) \\
&= -\frac{\mu_0}{\pi} \frac{Ia}{L} \frac{k}{2\sqrt{a\rho}} \int_0^{\frac{\pi}{2}} \frac{1-2\sin^2\theta}{\sqrt{1-k^2\sin^2\theta}} d\theta \\
&= -\frac{\mu_0}{\pi} \frac{I}{L} \frac{k}{2} \sqrt{\frac{a}{\rho}} \left[ K(k^2) - \frac{2}{k^2} \{K(k^2) - E(k^2)\} \right] \\
&= -\frac{\mu_0}{\pi} \frac{I}{L} \sqrt{\frac{a}{\rho}} \left( \frac{k^2-2}{2k} K(k^2) + \frac{1}{k} E(k^2) \right)_{\zeta-}^{\zeta+}
\end{aligned} \tag{A. 18}$$

※ 17.3. Complete Elliptic Integrals of the First and Second Kinds

$$K(x^2) = \int_0^{\frac{\pi}{2}} \frac{1}{\sqrt{1-x^2\sin^2\theta}} d\theta$$

$$E(x^2) = \int_0^{\frac{\pi}{2}} \sqrt{1-x^2\sin^2\theta} d\theta$$

$$\int_0^{\frac{\pi}{2}} \frac{\sin^2\theta}{\sqrt{1-x^2\sin^2\theta}} d\theta = \frac{1}{x^2} (K(x^2) - E(x^2))$$

$B_z$  can be obtained from (A. 3)

$$B_z = \frac{1}{r} \frac{\partial(rA_\phi)}{\partial\rho} = \frac{1}{r} A_\phi + \frac{\partial A_\phi}{\partial\rho} \quad (\text{A. 19})$$

For convenience

$$A_\phi = \frac{\mu_0}{2\pi} \frac{Ia}{L} \left[ \int_0^\pi \cos\phi' \cdot \ln(\zeta + \alpha(\zeta)) d\phi' \right]_{\zeta_-}^{\zeta_+} \quad (\text{A. 6})$$

$$\text{where, } \alpha(\zeta) = \sqrt{\zeta^2 + a^2 + \rho^2 - 2a\rho \cos\phi'}.$$

Calculate the derivative of (A. 19)

$$\frac{\partial A_\phi}{\partial\rho} = \frac{\mu_0}{2\pi} \frac{Ia}{L} \left[ \int_0^\pi \cos\phi' \cdot \frac{\partial}{\partial\rho} \ln(\zeta + \alpha(\zeta)) d\phi' \right]_{\zeta_-}^{\zeta_+} \quad (\text{A. 20})$$

Simplifying the differential term of the natural log in the above equation is

$$\begin{aligned} & \frac{\partial}{\partial\rho} \ln(\zeta + \alpha(\zeta)) \\ &= \frac{1}{\zeta + \alpha(\zeta)} \cdot \frac{1}{2} \left( \zeta^2 + \rho^2 + a^2 - 2a\rho \cos\phi' \right)^{-\frac{1}{2}} \cdot (2\rho - 2a \cos\phi') \\ &= \frac{1}{\zeta + \alpha(\zeta)} \cdot \frac{1}{2} \frac{1}{\alpha(\zeta)} \cdot (2\rho - 2a \cos\phi') \\ &= \frac{\rho - a \cos\phi'}{(\zeta + \alpha(\zeta)) \cdot \alpha(\zeta)} \end{aligned} \quad (\text{A. 21})$$

Using the same trick

$$\begin{aligned}
& \frac{\rho - a \cos \phi'}{(\zeta + \alpha(\zeta)) \cdot \alpha(\zeta)} \cdot \frac{(\alpha(\zeta) - \zeta)}{(\alpha(\zeta) - \zeta)} \\
&= \frac{(\rho - a \cos \phi')(\alpha(\zeta) - \zeta)}{(\alpha^2(\zeta) - \zeta^2)\alpha(\zeta)} \\
&= \frac{(\rho - a \cos \phi')(\alpha(\zeta) - \zeta)}{\alpha(\zeta)(\rho^2 + a^2 - 2a\rho \cos \phi')} \\
&= \frac{(\rho - a \cos \phi')}{(\rho^2 + a^2 - 2a\rho \cos \phi')} + \frac{-(\rho - a \cos \phi')\zeta}{\alpha(\zeta)(\rho^2 + a^2 - 2a\rho \cos \phi')} \tag{A. 22}
\end{aligned}$$

Therefore:

$$\frac{\partial A_\phi}{\partial \rho} = \frac{\mu_0}{2\pi} \frac{Ia}{L} \left[ \int_0^\pi \cos \phi' \cdot \frac{-(\rho - a \cos \phi')\zeta}{\alpha(\zeta)(\rho^2 + a^2 - 2a\rho \cos \phi')} d\phi' \right]_{\zeta_-}^{\zeta_+} \tag{A. 23}$$

Combined with

$$\frac{1}{\rho} A_\phi = \frac{\mu_0}{2\pi} \frac{Ia}{L} \left[ \int_0^\pi \frac{a\zeta \sin^2 \phi'}{\alpha(\zeta)(\rho^2 + a^2 - 2a\rho \cos \phi')} d\phi' \right]_{\zeta_-}^{\zeta_+}$$

Then the magnetic field is

$$B_z = \frac{\mu_0}{2\pi} \frac{Ia}{L} \left[ \int_0^\pi \frac{a\zeta - \rho\zeta \cos \phi'}{\alpha(\zeta)(\rho^2 + a^2 - 2a\rho \cos \phi')} d\phi' \right]_{\zeta_-}^{\zeta_+} \tag{A. 24}$$

With change the interval

$$\begin{aligned}
& \int_0^\pi \frac{a\zeta - \rho\zeta \cos\phi'}{\alpha(\zeta)(\rho^2 + a^2 - 2a\rho \cos\phi')} d\phi' \\
&= \int_0^\pi \frac{a\zeta - \rho\zeta \cos\phi'}{(\rho^2 + a^2 - 2a\rho \cos\phi')\sqrt{\zeta^2 + \rho^2 + a^2 - 2a\rho \cos\phi'}} d\phi' \\
&= \int_0^{\frac{\pi}{2}} \frac{a\zeta + \rho\zeta \cos\phi'}{(a^2 + \rho^2 + 2a\rho \cos\phi')\sqrt{\zeta^2 + a^2 + \rho^2 + 2a\rho \cos\phi'}} (-d\phi') \\
&= - \int_0^{\frac{\pi}{2}} \frac{a\zeta + \rho\zeta \cos 2\theta}{((a+\rho)^2 - 4a\rho \sin^2 \theta)\sqrt{\zeta^2 + (a+\rho)^2 - 4a\rho \sin^2 \theta}} (2d\theta)
\end{aligned} \tag{A. 25}$$

$$\text{let } h^2 = \frac{4a\rho}{(a+\rho)^2}, \ k^2 = \frac{4a\rho}{(a+\rho)^2 + \zeta^2}$$

$$\begin{aligned}
& - \int_0^{\frac{\pi}{2}} \frac{a\zeta + \rho\zeta \cos 2\theta}{((a+\rho)^2 - 4a\rho \sin^2 \theta)\sqrt{\zeta^2 + (a+\rho)^2 - 4a\rho \sin^2 \theta}} (2d\theta) \\
&= - \frac{kh^2}{4(\sqrt{a\rho})^3} \int_0^{\frac{\pi}{2}} \frac{(a+\rho)\zeta - 2\rho\zeta \sin^2 \theta}{(1-h^2 \sin^2 \theta)\sqrt{1-k^2 \sin^2 \theta}} d\theta
\end{aligned} \tag{A. 28}$$

$$\begin{aligned}
& \int_0^{\frac{\pi}{2}} \frac{\sin^2 \phi}{(1-h^2 \sin^2 \phi)\sqrt{1-k^2 \sin^2 \phi}} d\phi \\
&= - \frac{1}{h^2} \int_0^{\frac{\pi}{2}} \frac{1-h^2 \sin^2 \phi - 1}{(1-h^2 \sin^2 \phi)\sqrt{1-k^2 \sin^2 \phi}} d\phi \\
&= \frac{1}{h^2} \int_0^{\frac{\pi}{2}} \frac{1}{(1-h^2 \sin^2 \phi)\sqrt{1-k^2 \sin^2 \phi}} - \frac{1}{\sqrt{1-k^2 \sin^2 \phi}} d\phi \\
&= \frac{1}{h^2} (\prod(h^2, k^2) - K(k^2))
\end{aligned} \tag{A. 29}$$

※ 17.7 Elliptic Integral of the Third Kind

$$\Pi(n, m) = \int_0^{\frac{\pi}{2}} \frac{1}{(1 - n \sin^2 \phi) \sqrt{1 - m \sin^2 \phi}} d\phi$$

$$\begin{aligned}
 &= -\frac{kh^2}{4(\sqrt{a\rho})^3} \left( (a+\rho)\zeta \Pi(h^2, k^2) - \frac{2\rho\zeta}{h^2} (\Pi(h^2, k^2) - K(k^2)) \right) \\
 &= -\frac{k}{4(\sqrt{a\rho})^3} \left( (h^2(a+\rho) - 2\rho)\zeta \Pi(h^2, k^2) + 2\rho\zeta K(k^2) \right) \\
 &= -\frac{k\zeta}{4(\sqrt{a\rho})^3} \left( 2\rho K(k^2) + \left( \frac{4a\rho}{a+\rho} - 2\rho \right) \Pi(h^2, k^2) \right) \\
 &= -\frac{k\zeta}{2a\sqrt{a\rho}} \left( K(k^2) + \frac{a-\rho}{a+\rho} \Pi(h^2, k^2) \right)
 \end{aligned} \tag{A. 30}$$

Finally, the  $B_z$  is summarized as follows.

$$\begin{aligned}
 B_z &= \frac{\mu_0 I a}{2\pi L} \left[ -\frac{k\zeta}{2a\sqrt{a\rho}} \left( K(k^2) + \frac{a-\rho}{a+\rho} \Pi(h^2, k^2) \right) \right]_{\zeta_-}^{\zeta_+} \\
 &= -\frac{\mu_0 I}{4\pi L \sqrt{a\rho}} \left[ k\zeta \left( K(k^2) + \frac{a-\rho}{a+\rho} \Pi(h^2, k^2) \right) \right]_{\zeta_-}^{\zeta_+}
 \end{aligned} \tag{A. 31}$$

$$\text{where, } h^2 = \frac{4a\rho}{(a+\rho)^2}, \quad k^2 = \frac{4a\rho}{(a+\rho)^2 + \zeta^2}.$$

## Expression Levels of ALDH1 and CD44+/CD24- during MFH treatment

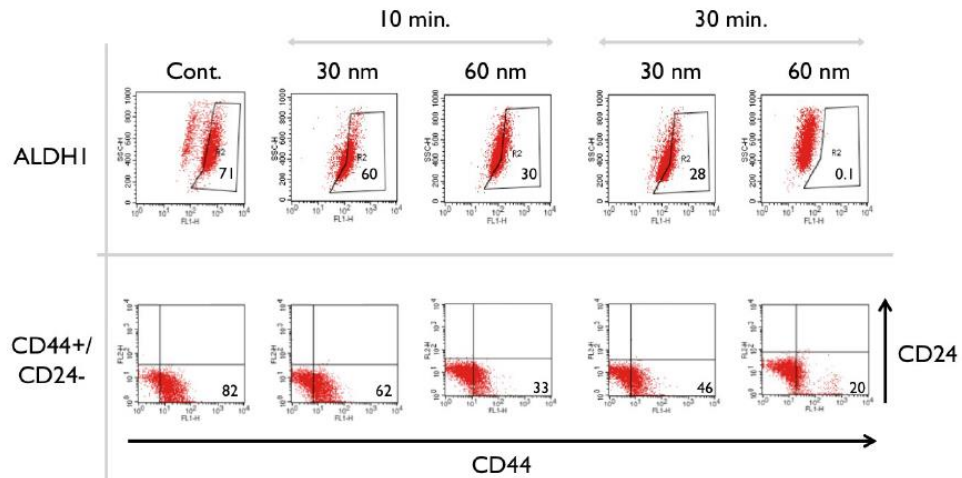


Fig. A2. The expression levels of the biomarkers.

The changes in the expression levels of the bCSC biomarkers during the magnetic hyperthermia were determined by flow cytometry. The intensity of ALDH1 and CD44+/CD24- expressions decreased (Fig. A2), which is consistent with the cell viability results (Fig. 19).

## Expression Levels of HSP70 and HSP90

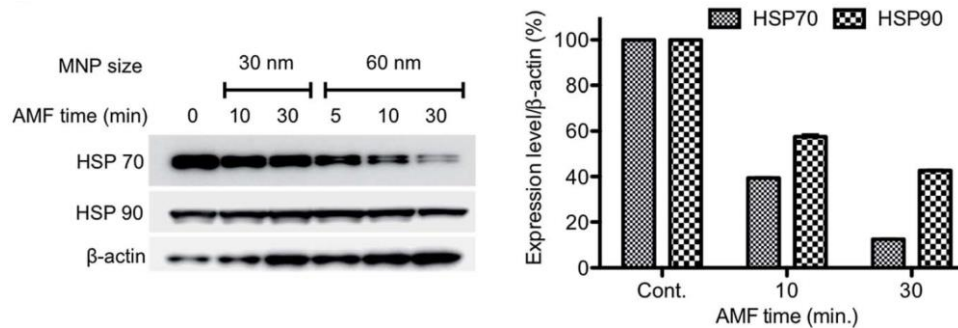


Fig. A3. Expression Levels of HSP70 and HSP90 proteins.

To understand the mechanism of cell death induced by thermal therapy, the expression levels of heat shock protein 70 and 90 (HSP70 and HSP90), which respond to thermal stress and provide transient thermo-tolerance to cells on exposure to heat stress, were determined by western blot analysis (Fig. A3). The expression levels of HSP70 and 90 were downregulated. The co-inhibition of HSP70/90, which protects against heat stress, accelerated the apoptosis process [76].

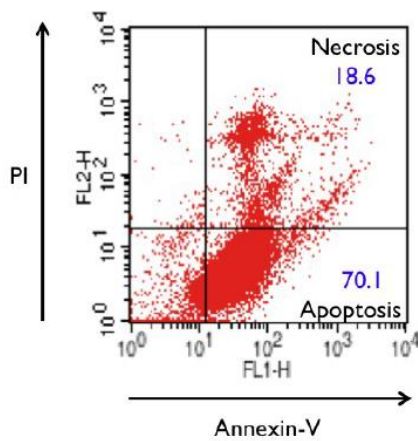


Fig. A4. Staining analysis with PI and annexin-V to establish the cell death process.

To further understand the apoptosis process, the treated cells were stained with annexin VFITC and PI (apoptosis kit, Invitrogen) and subjected to flow cytometry (Fig. S5b†). The results indicated that the 60 nm sized MNC generated enough heat and thermal stress to promote the thermal apoptosis process under the AMF conditions.

## References

1. Okoniewski, M. and M.A. Stuchly, *A study of the handset antenna and human body interaction.* Ieee Transactions on Microwave Theory and Techniques, 1996. **44**(10): p. 1855-1864.
2. VanderVorst, A. and F. Duhamel, *1990-1995 advances in investigating the interaction of microwave fields with the nervous system.* Ieee Transactions on Microwave Theory and Techniques, 1996. **44**(10): p. 1898-1909.
3. Apollonio, F., G. D'Inzeo, and L. Tarricone, *Theoretical analysis of voltage-gated membranechannels under GSM and DECT exoposure,* in *IEEE MTT-S Int. Microwave Symp. Dig.* 1997: Denver.
4. Michaelson, S. and J.C. Lin, *Biological Effectss and Health Implications of Radio-Frequency Radiation.* 1987, New York: Plenum.
5. Thuery, J., *Microwaves-Industrial, Scientific and Medical Applications.* 1992, Norwood, MA: Artech House.
6. Polk, C. and E. Postow, *Handbook of Biological Effects of Electromagnetic Fields.* 1996, Boca Raton, FL: CRC Press.
7. Vorst, A.V. *Microwave bioelectromagnetics in Europe.* in *IEEE MTT-S Int. Microwave Symp. Dig.* 1993. Atlanta, GA.
8. Roosen, A. and H.D. Rosen, *New Frontiers in Medical Device Technology.* 1995, New York: Wiley.
9. Sadhukha, T., et al., *Effective Elimination of Cancer Stem Cells by Magnetic Hyperthermia.* Molecular Pharmaceutics, 2013. **10**(4): p. 1432-1441.
10. Yin, P.T., et al., *Stem cell-based gene therapy activated using magnetic*

*hyperthermia to enhance the treatment of cancer.* Biomaterials, 2016. **81**: p. 46-57.

11. Pineiro-Redondo, Y., et al., *The influence of colloidal parameters on the specific power absorption of PAA-coated magnetite nanoparticles.* Nanoscale Res Lett, 2011. **6**(1): p. 383.
12. Kievit, F.M. and M. Zhang, *Surface engineering of iron oxide nanoparticles for targeted cancer therapy.* Acc Chem Res, 2011. **44**(10): p. 853-62.
13. Khandhar, A.P., R.M. Ferguson, and K.M. Krishnan, *Monodispersed magnetite nanoparticles optimized for magnetic fluid hyperthermia: Implications in biological systems.* J Appl Phys, 2011. **109**(7): p. 7B310-7B3103.
14. Dutz, S., et al., *Magnetic multicore nanoparticles for hyperthermia-influence of particle immobilization in tumour tissue on magnetic properties.* Nanotechnology, 2011. **22**(26).
15. Blanco-Andujar, C., et al., *High performance multi-core iron oxide nanoparticles for magnetic hyperthermia: microwave synthesis, and the role of core-to-core interactions.* Nanoscale, 2015. **7**(5): p. 1768-1775.
16. Mohapatra, J., et al., *Enhancement of magnetic heating efficiency in size controlled MFe<sub>2</sub>O<sub>4</sub> (M = Mn, Fe, Co and Ni) nanoassemblies.* Rsc Advances, 2015. **5**(19): p. 14311-14321.
17. Kwon, Y.S., et al., *Optimization of magnetic hyperthermia effect for breast cancer stem cell therapy.* Rsc Advances, 2016. **6**(109): p. 107298-107304.
18. Cha, J., et al., *Relaxivity control of magnetic nanoclusters for efficient magnetic relaxation switching assay.* Chemical Communications, 2013. **49**(5): p. 457-459.

19. Jeun, M., et al., *Physical limits of pure superparamagnetic Fe<sub>3</sub>O<sub>4</sub> nanoparticles for a local hyperthermia agent in nanomedicine*. Applied Physics Letters, 2012. **100**(9).
20. Khandhar, A.P., R.M. Ferguson, and K.M. Krishnan, *Monodispersed magnetite nanoparticles optimized for magnetic fluid hyperthermia: Implications in biological systems*. Journal of Applied Physics, 2011. **109**(7).
21. Rosensweig, R.E., *Heating magnetic fluid with alternating magnetic field*. Journal of Magnetism and Magnetic Materials, 2002. **252**(1-3): p. 370-374.
22. Deatsch, A.E. and B.A. Evans, *Heating efficiency in magnetic nanoparticle hyperthermia*. Journal of Magnetism and Magnetic Materials, 2014. **354**: p. 163-172.
23. Kobayashi, H., et al., *Self-heating property under ac magnetic field and its evaluation by ac/dc hysteresis loops of NiFe<sub>2</sub>O<sub>4</sub> nanoparticles*. Journal of Applied Physics, 2010. **107**(9).
24. Kobayashi, H., et al., *Self-Heating Property of Magnetite Nanoparticles Dispersed in Solution*. Ieee Transactions on Magnetics, 2011. **47**(10): p. 4151-4154.
25. Nakamura, K., et al., *Self-Heating Temperature and AC Hysteresis of Magnetic Iron Oxide Nanoparticles and Their Dependence on Secondary Particle Size*. Ieee Transactions on Magnetics, 2013. **49**(1): p. 240-243.
26. Cheng, *Field and Wave Electromagnetics*.
27. Jackson, *Classical Electrodynamics*.
28. JP, A., *Power electronic systems: Theory and Design*. 2001.
29. Ahamed, M., et al., *Oxidative stress mediated apoptosis induced by nickel ferrite nanoparticles in cultured A549 cells*. Toxicology, 2011. **283**(2-3): p.

- 101-8.
30. Mehdaoui, B., et al., *Increase of magnetic hyperthermia efficiency due to dipolar interactions in low-anisotropy magnetic nanoparticles: Theoretical and experimental results*. Physical Review B, 2013. **87**(17).
  31. Attar, M.M., et al., *Thermal analysis of magnetic nanoparticle in alternating magnetic field on human HCT-116 colon cancer cell line*. International Journal of Hyperthermia, 2016. **32**(8): p. 858-867.
  32. Begamudre, R.D., *Electromechanical Energy Conversion with Dynamics of Machines*.
  33. Atkinson, W.J., I.A. Brezovich, and D.P. Chakraborty, *Usable Frequencies in Hyperthermia with Thermal Seeds*. Ieee Transactions on Biomedical Engineering, 1984. **31**(1): p. 70-75.
  34. Dontu, G., et al., *In vitro propagation and transcriptional profiling of human mammary stem/progenitor cells*. Genes Dev, 2003. **17**(10): p. 1253-70.
  35. Lin, L., et al., *STAT3 is necessary for proliferation and survival in colon cancer-initiating cells*. Cancer Res, 2011. **71**(23): p. 7226-37.
  36. Oh, B.Y., R.A. Lee, and K.H. Kim, *siRNA targeting Livin decreases tumor in a xenograft model for colon cancer*. World Journal of Gastroenterology, 2011. **17**(20): p. 2563-2571.
  37. Gradinaru, V., et al., *Optical deconstruction of parkinsonian neural circuitry*. Science, 2009. **324**(5925): p. 354-9.
  38. Greenberg, B.D., et al., *Deep brain stimulation of the ventral internal capsule/ventral striatum for obsessive-compulsive disorder: worldwide experience*. Mol Psychiatry, 2010. **15**(1): p. 64-79.
  39. Tufail, Y., et al., *Transcranial pulsed ultrasound stimulates intact brain*

- circuits*. Neuron, 2010. **66**(5): p. 681-94.
40. Hallett, M., *Transcranial magnetic stimulation and the human brain*. Nature, 2000. **406**(6792): p. 147-50.
  41. Merrill, D.R., M. Bikson, and J.G. Jefferys, *Electrical stimulation of excitable tissue: design of efficacious and safe protocols*. J Neurosci Methods, 2005. **141**(2): p. 171-98.
  42. Histed, M.H., V. Bonin, and R.C. Reid, *Direct activation of sparse, distributed populations of cortical neurons by electrical microstimulation*. Neuron, 2009. **63**(4): p. 508-22.
  43. Rossi, S., et al., *Safety, ethical considerations, and application guidelines for the use of transcranial magnetic stimulation in clinical practice and research*. Clin Neurophysiol, 2009. **120**(12): p. 2008-39.
  44. Rossini, P.M., et al., *Non-invasive electrical and magnetic stimulation of the brain, spinal cord, roots and peripheral nerves: Basic principles and procedures for routine clinical and research application. An updated report from an I.F.C.N. Committee*. Clin Neurophysiol, 2015. **126**(6): p. 1071-107.
  45. Lefaucheur, J.P., et al., *Evidence-based guidelines on the therapeutic use of repetitive transcranial magnetic stimulation (rTMS)*. Clin Neurophysiol, 2014. **125**(11): p. 2150-206.
  46. Fitzgerald, P.B., S. Fountain, and Z.J. Daskalakis, *A comprehensive review of the effects of rTMS on motor cortical excitability and inhibition*. Clin Neurophysiol, 2006. **117**(12): p. 2584-96.
  47. Nitsche, M.A. and W. Paulus, *Excitability changes induced in the human motor cortex by weak transcranial direct current stimulation*. J Physiol, 2000. **527 Pt 3**: p. 633-9.

48. Nitsche, M.A., et al., *Transcranial direct current stimulation: State of the art* 2008. Brain Stimul, 2008. **1**(3): p. 206-23.
49. Valiengo, L.C., et al., *Transcranial direct current stimulation and repetitive transcranial magnetic stimulation in consultation-liaison psychiatry*. Braz J Med Biol Res, 2013. **46**(10): p. 815-23.
50. Priori, A., M. Hallett, and J.C. Rothwell, *Repetitive transcranial magnetic stimulation or transcranial direct current stimulation?* Brain Stimul, 2009. **2**(4): p. 241-5.
51. Miranda, P.C., M. Lomarev, and M. Hallett, *Modeling the current distribution during transcranial direct current stimulation*. Clin Neurophysiol, 2006. **117**(7): p. 1623-9.
52. Siebner, H.R., et al., *How does transcranial magnetic stimulation modify neuronal activity in the brain? Implications for studies of cognition*. Cortex, 2009. **45**(9): p. 1035-42.
53. Rosen, A., M.A. Stuchly, and A. Vander Vorst, *Applications of RF/microwaves in medicine*. Ieee Transactions on Microwave Theory and Techniques, 2002. **50**(3): p. 963-974.
54. Grossman, N., et al., *Noninvasive Deep Brain Stimulation via Temporally Interfering Electric Fields*. Cell, 2017. **169**(6): p. 1029-+.
55. Li, H.D., et al., *Low-intensity (400 mW/cm<sup>2</sup>, 500 kHz) pulsed transcranial ultrasound preconditioning may mitigate focal cerebral ischemia in rats*. Brain Stimulation, 2017. **10**(3): p. 695-702.
56. Beason, R.C. and P. Semm, *Responses of neurons to an amplitude modulated microwave stimulus*. Neuroscience Letters, 2002. **333**(3): p. 175-178.
57. Roggeveen, S., J. van Os, and R. Lousberg, *Does the Brain Detect 3G*

*Mobile Phone Radiation Peaks? An Explorative In-Depth Analysis of an Experimental Study.* Plos One, 2015. **10**(5).

58. Hutcheon, B. and Y. Yarom, *Resonance, oscillation and the intrinsic frequency preferences of neurons.* Trends in Neurosciences, 2000. **23**(5): p. 216-222.
59. Huang, Y.Z., et al., *Theta burst stimulation of the human motor cortex.* Neuron, 2005. **45**(2): p. 201-6.
60. Paxinos, G. and K.B.J. Franklin, *The mouse brain in stereotaxic coordinates.* 2001, San Diego: Academic Press.
61. Trippe, J., et al., *Theta burst and conventional low-frequency rTMS differentially affect GABAergic neurotransmission in the rat cortex.* Experimental Brain Research, 2009. **199**(3-4): p. 411-421.
62. Benali, A., et al., *Theta-Burst Transcranial Magnetic Stimulation Alters Cortical Inhibition.* Journal of Neuroscience, 2011. **31**(4): p. 1193-1203.
63. Dobkin, B.H., *The Clinical Science of Neurologic Rehabilitation.* 2003, New York: Oxford.
64. Mayberg, H.S., et al., *Deep brain stimulation for treatment-resistant depression.* Neuron, 2005. **45**(5): p. 651-660.
65. Park, U., *Wideband power divider using a coaxial cable 2:1 transmission line transformer.* Ieice Electronics Express, 2010. **7**(8): p. 534-538.
66. Blackham, D.V. and R.D. Pollard, *An improved technique for permittivity measurements using a coaxial probe.* Ieee Transactions on Instrumentation and Measurement, 1997. **46**(5): p. 1093-1099.
67. Kim, E.J., et al., *Amygdalar Stimulation Produces Alterations on Firing Properties of Hippocampal Place Cells.* Journal of Neuroscience, 2012.

- 32**(33): p. 11424-11434.
- 68. Seo, T., et al., *Noninvasive Brain Stimulation Using a Modulated Microwave Signal*. Journal of Electromagnetic Engineering and Science, 2018. **18**(1): p. 70-72.
  - 69. Ham, D. and A. Hajimiri, *Concepts and methods in optimization of integrated LC VCOs*. Ieee Journal of Solid-State Circuits, 2001. **36**(6): p. 896-909.
  - 70. Arias-Gil, G., et al., *Measurement, modeling, and prediction of temperature rise due to optogenetic brain stimulation*. Neurophotonics, 2016. **3**(4): p. 045007.
  - 71. Deng, W., et al., *Optogenetics, the intersection between physics and neuroscience: light stimulation of neurons in physiological conditions*. Am J Physiol Regul Integr Comp Physiol, 2014. **307**(11): p. R1292-302.
  - 72. Thomsen, S., *Pathologic analysis of photothermal and photomechanical effects of laser-tissue interactions*. Photochem Photobiol, 1991. **53**(6): p. 825-35.
  - 73. Kim, N., et al. *High-power reflection coefficient measurement of biological material applicable to microwave hyperthermia*. in *Microwave Symposium Digest*. 2009.
  - 74. Jung, D., et al., *Conditional Knockout of Cav2.1 Disrupts the Accuracy of Spatial Recognition of CA1 Place Cells and Spatial/Contextual Recognition Behavior*. Frontiers in Behavioral Neuroscience, 2016. **10**.
  - 75. Makowiecki, K., et al., *Low-Intensity Repetitive Transcranial Magnetic Stimulation Improves Abnormal Visual Cortical Circuit Topography and Upregulates BDNF in Mice*. Journal of Neuroscience, 2014. **34**(32): p.

10780-10792.

76. Cui, X.B., et al., *Co-inhibition of HSP70/HSP90 synergistically sensitizes nasopharyngeal carcinoma cells to thermotherapy*. Integr Cancer Ther, 2012. **11**(1): p. 61-7.

## Abstract in Korean (국문초록)

본 논문에서는 RF/マイクロ波의 응용 분야로서 자성 유체 온열 및 뇌 자극에 관한 연구를 수행하였습니다.

첫 번째 장에서는 자성 유체 온열요법 (MFH)이 연구되었습니다. 규칙적인 크기 분포와 높은 안정성을 가진 자성, 산화철, 나노 클러스터 (MNC)가 성공적으로 준비되었습니다. MNC의 치료 효과를 높이기 위해 입자 크기 분포, 외부 자기장 빈도 및 강도와 같은 다양한 요인에 따라 최적 조건을 찾는 과정이 있었습니다. 열 발생 능력과 다양한 요인 사이의 상관관계는 특정 손실 전력 (SLP)을 측정하여 평가되었습니다. 60 nm MNC는 다양한 자기장 조건에서 가장 높은 열용량을 보였습니다. chemo/radio-resistance가 있는 유방암 줄기세포 (bCSCs)를 MNC로 처리 후 최적화된 교류 자기장에 노출되었습니다. MNC는 10분 이내에 적절한 온도 상승을 촉진했습니다. 그 결과 CSCs는 세포 자멸사로 진행되었습니다.

MFH 치료를 위해 MNC가 생체 조직에 주입되는 경우, 세포 및 생체 내 실험은 신진대사, 혈액량 또는 속도 때문에 세포실험과 같은 효과를 보장할 수 없습니다. MFH에 적합한 MNC를 누드 마우스 종양 조직의 중간에 직접 주사했습니다. MNC를 둘러싼 미세 환경이 변경되었기 때문에 자기장 조건을 치료 효과를 얻기 위해 변경하였습니다. 자기장의 강도는 치료하고자 하는 조직의 온도 변화에 따라 변합니다. MFH 치료 후 종양 부피가 감소하는 것으로 나타났습니다. 그러나 모든 종양 조직이 치료되지는 않았습니다. 치료 효과를 높이기 위해 다른 마우스를 이용하여 암 조직의 여러 부위에 MNC를 주사했다. 그 결과, 건강한 조직에 손

상을 주지 않으면서 중앙 조직만 없어지는 것이 육안으로 확인되었습니다.

두 번째 연구로서, 전자기장을 이용한 신경 자극의 결과가 제시됩니다. 풀 브리지 인버터 회로를 사용하여 기존의 경 두개 자기 자극 (TMS) 시스템을 향상했습니다. 제안된 TMS 시스템은 펠스 폭을 제어하고 복잡한 뇌 자극 프로토콜을 생성할 수 있습니다. 시상하부 버스트 발화 패턴을 모방한 새로운 TMS 프로토콜을 내인성 시상피질(TC) 활성에 대해 시험 하였습니다. TMS 적용 후 통증 행동이 감소함을 확인했습니다.

제안된 TMS 시스템은 연속 신호의 포락선을 변조하여 버스트 발사 패턴을 생성했습니다. 엔벨로프 변조된 마이크로파 신호가 뉴런의 발사 속도에 영향을 미치는지에 대하여 연구를 계속하였습니다. 마이크로파는 전자기장 분포를 좁히고 TMS와 같은 기존의 뇌 자극 방법보다 적은 전력으로 뇌 활동을 조절할 수 있게 했습니다. 뇌 자극 시스템의 마이크로파 회로는 MMIC 기술과 반도체 제조 공정에 의해 개발되었습니다. 생체 내 실험은 반복적인 펠스 엔벨로프를 갖는 마이크로파 신호가 개별 뉴런의 활동을 성공적으로 변화시켰음을 확인했습니다.

이 논문에서는 RF/마이크로파가 에너지 전환 제제인 MNC를 통해 생물 조직의 온도를 상승시킬 수 있음을 보여 주었습니다. 이를 통해 암 치료의 보조적인 수단으로 활용을 기대합니다. 또한, 신호의 변조를 통해 뇌 활동 제어에 실질적으로 적용할 수 있는 수단을 제공하였습니다.

핵심어 : 자기 유체 온열요법, 자성 나노입자, 자기장 발생기, 경두개자기 자극, 신경조절, 비 침습적 뇌 자극, 마이크로파 뇌 자극, 자극 어플리케이터

학번 : 2011-30963